L. Morcillo-Montalbá and M. Rodrigo-Gámiz contributed equally to this work.

Key Points:

- Four independent lipid-based paleothermometers are applied in the westernmost Mediterranean
- High-resolution sea surface temperature records reveal abrupt changes during Dansgaard-Oeschger and Heinrich events over the last 35 kyr
- Elevated accumulation rates of lipid biomarkers are recorded during Dansgaard-Oeschger interstadials

Rapid Climate Changes in the Westernmost Mediterranean (Alboran Sea) Over the Last 35 kyr: New Insights From Four Lipid Paleothermometers ($U^{K'}_{37}$, TEX^{H}_{86}, RI-OH', and LDI)

L. Morcillo-Montalbá[1] , M. Rodrigo-Gámiz[2] , F. Martínez-Ruiz[1] , M. Ortega-Huertas[3] , S. Schouten[4,5], and J. S. Sinninghe Damsté[4,5]

[1]Andalusian Institute of Earth Sciences (IACT), CSIC-University of Granada, Granada, Spain, [2]Department of Stratigraphy and Paleontology, University of Granada, Granada, Spain, [3]Department of Mineralogy and Petrology, University of Granada, Granada, Spain, [4]Department of Marine Microbiology and Biogeochemistry, NIOZ Royal Netherlands Institute of Sea Research, Den Burg, The Netherlands, [5]Department of Earth Sciences, Faculty of Geosciences, Utrecht University, Utrecht, The Netherlands

Abstract The westernmost Mediterranean is one of the most sensitive areas to global climate change and high sedimentation rates allow recording high frequency variability. We present a high-resolution paleotemperature reconstruction over the last 35 kyr using, for the first time, four independent organic sea surface temperature (SST) proxies ($U^{K'}_{37}$, TEX^{H}_{86}, RI-OH' and LDI) based on alkenones, (hydroxy) isoprenoid GDGTs, and long-chain diols. We also generated a $\delta^{18}O$ of planktonic foraminifera *G. bulloides* record together with records of bulk parameters (total organic carbon content, $\delta^{13}C_{org}$) and the accumulation rates of different biomarkers to provide insights into terrestrial input and primary producers. All derived-SST records showed similar trends over the last 35 kyr, revealing abrupt temperature variations during the last seven Dansgaard-Oeschger (D/O) cycles, the three Heinrich (H) events, the Last Glacial Maximum, and the Younger Dryas. H3 is recognized as the coldest event, while H1 was recorded by all SST proxies as the most abrupt one. In general, TEX^{H}_{86}-, RI-OH'- and LDI-SST estimates were lower than those obtained from $U^{K'}_{37}$. The LDI paleothermometer recorded the largest range of absolute SSTs over the whole period (ca. 20°C) followed by RI-OH' (ca. 16°C). TEX^{H}_{86}, RI-OH' and LDI proxies reflected sudden SST changes during the D/O 6 and 5 particularly well. Low BIT values and the abundance of C_{32} 1,15-diol in range with typical marine values indicated only minor input of continental organic matter. Accumulation rates of different lipid biomarkers were generally modulated by D/O cycles, suggesting enhanced productivity during D/O interstadials and the Bölling-Alleröd period.

1. Introduction

Glacial/interglacial transitions are particularly important to assess climate variability (e.g., Lang & Wolff, 2011) since their specific environmental conditions and forcing mechanisms may shed light on the present climate variability and future climate scenarios. High-frequency climatic instabilities during the last glacial period are known as the Dansgaard/Oeschger (D/O) cycles (Bond et al., 1993; Dansgaard et al., 1993), which are characterized as rapid warming (interstadial) and gradual cooling (stadial) episodes culminating with the anomalous occurrence of ice-rafted detritus and large-scale destabilization of the circum-North Atlantic ice sheets defined as Heinrich events (H) (Heinrich, 1988; Hemming, 2004). Particularly, the last 35 kyr involved several abrupt climatic and oceanographic episodes, that is, seven D/O cycles (stadials/interstadials), the last three H events (H3, H2, H1), the Last Glacial Maximum (LGM), the Bölling-Alleröd (B-A), and the Younger Dryas (YD) (Bond et al., 1992, 1993; Broecker, 1994; Clark et al., 2012; Dansgaard et al., 1993; Heinrich, 1988; Hemming, 2004; Johnsen et al., 2001). In order to constrain such variations, expanded marine records are required to allow high-resolution studies of these climate events, thus providing new insights into the mechanisms and forces of rapid climate changes.

The Mediterranean Sea is highly sensitive to climate oscillations due to its semi-enclosed nature and its latitudinal location (e.g., Krijgsman, 2002), and hence forms a natural laboratory for such paleoclimate reconstructions. The unique characteristics of the Mediterranean in terms of climate and oceanographic conditions have led to numerous reconstructions based on a diverse set of paleoenvironmental proxies (e.g., Abrantes et al., 2012; Lionello, 2012; Martínez-Ruiz et al., 2015). In particular, the westernmost Mediterranean (Alboran Sea) is an exceptional location since high sedimentation rates have provided excellent records for reconstructing past climate

variability at high-resolution. Studies were based on geochemical proxies (e.g., Cacho et al., 1999, 2001, 2002; Martrat et al., 2004, 2014; Moreno et al., 2005; Rodrigo-Gámiz et al., 2011, 2014), on pollen records (e.g., Combourieu Nebout et al., 2009; Fletcher & Sánchez Goñi, 2008), or were focused on variations in the abundance of specific microfossil assemblages (e.g., Ausín et al., 2015; Bazzicalupo et al., 2018; Incarbona et al., 2013; Pérez-Asensio et al., 2020). Sea surface temperature (SST) is a parameter that is highly sensitive to climate variability and past abrupt climate changes. To date, paleotemperature studies aimed at the reconstruction of past SST in the western Mediterranean have been focused on the application of diverse proxies including the Mg/Ca ratio of benthic and planktonic foraminifera (e.g., Boussetta et al., 2012; Cacho et al., 2006; Català et al., 2019) and specific biomarkers (e.g., Cacho et al., 2002, 1999; Davtian et al., 2019; Kim et al., 2015; Martrat et al., 2004; Nieto-Moreno et al., 2013; Rodrigo-Gámiz et al., 2014), that is, fossil organic molecules derived from a specific biological source.

The first biomarker-based SST proxy, the $U^{K'}_{37}$ index (Brassell et al., 1986), has been widely applied over several decades. It is based on the ratio between C_{37} di- and tri-unsaturated alkenones (Prahl & Wakeman, 1987) synthesized by a specific group of the haptophyte algae, such as *Emiliania huxleyi* (Volkman, Eglinton, Corner, & Forsberg, 1980; Volkman, Eglinton, Corner & Sargent, 1980), and is strongly related to annual mean SST (Müller et al., 1998). The $U^{K'}_{37}$ index can be affected by diagenesis (Gong & Hollander, 1999; Hoefs et al., 1998), salinity changes (Schulz et al., 2000), or physiological growth (nutrient and light limitation) (Herbert, 2003; Versteegh et al., 2001). Numerous studies have used the $U^{K'}_{37}$ index to globally reconstruct SSTs, including the Mediterranean Sea (e.g., Cacho et al., 2001; Castañeda et al., 2010; Huguet et al., 2011; Martrat et al., 2004, 2014). For the latter, a specific $U^{K'}_{37}$ calibration was proposed since a study of suspended particulate matter from the northwestern Mediterranean showed a bias in derived-SST using the general calibration (Ternois et al., 1997). Nevertheless, the application of global calibrations (Müller et al., 1998) has shown good results in the sedimentary record (e.g., Cacho et al., 1999).

The TEX_{86} index (Schouten et al., 2002) is another organic temperature proxy that is based on the correlation of the relative abundance of specific isoprenoid glycerol dialkyl glycerol tetraethers (isoGDGTs) with annual mean SST (Kim et al., 2010). IsoGDGTs (containing 0–3 cyclopentane moieties), crenarchaeol (Cren) (containing four cyclopentane moieties and a cyclohexane moiety), and the crenarchaeol isomer (Cren') are biosynthesized by Thaumarchaeota (Sinninghe Damsté, Schouten, et al., 2002), which are chemoautotrophic (ammonia-oxidizing) archaea (Könneke et al., 2005; Wuchter et al., 2006). Hence, their occurrence is not limited to the photic zone and they occur in oceanic waters at depths >1,000 m (Karner et al., 2001). This has been demonstrated for the Mediterranean Sea, where surface sediments at depths >1,000 m were shown to have received a contribution of isoGDGTs from deep-water dwelling Thaumarchaeota (Besseling et al., 2019; Kim et al., 2015), revealing that these sediments may reflect signals related to the whole water column. Nevertheless, for these surface sediments from depths >1,000 m, the correlation of TEX^{H}_{86} values (expressed as $\log(TEX_{86})$ by Kim et al., 2010) with satellite-derived annual mean SST is different from the global core-top calibration, being much stronger than with water column-integrated temperatures (Kim et al., 2015). The TEX^{H}_{86} proxy is not dependent on changes in salinity and nutrients (Elling et al., 2015; Wuchter et al., 2004) and is less affected by diagenesis than the $U^{K'}_{37}$ index (Kim et al., 2009; Schouten et al., 2004). TEX_{86}-derived SST reconstructions can, however, be biased by GDGTs derived from the continent (Weijers et al., 2006). In marine settings this can be assessed with the Branched and Isoprenoid Tetraether (BIT) index (Hopmans et al., 2004, 2016), which uses the abundance of branched GDGTs (brGDGTs), thought to be mainly derived from the continent, relative to crenarchaeol, mainly marine-derived. Besides these GDGTs, isoGDGTs containing one or two hydroxyl groups (i.e., OH-GDGTs) have also been reported to widely occurring in marine surface sediments (e.g., Liu et al., 2012). Although their biological source is less well established, culture studies point to Thaumarchaeota Group 1.1a (e.g., *Nitrosopumilus maritimus*), SAGMCG-1 (e.g., *Nitrosotalea devanaterra*) (Elling et al., 2017; Liu et al., 2012), and thermophilic Euryarchaeota (i.e., *Methanothermococcus thermolithotrophicus*; Liu et al., 2012) as potential biological sources. A combined lipidomic and 16S rRNA gene amplicon sequencing approach revealed that in the Black Sea OH-GDGTs are produced by Thaumarchaeota Group 1.1a and not by Euryarchaeota (Sollai et al., 2019). In a set of globally distributed marine sediment records, the distribution of OH-GDTGs is correlated to SST (de Bar, Dorhout, et al., 2019; Davtian et al., 2019; Fietz et al., 2013, 2020; Huguet et al., 2013). In particular, the ring index of OH-GDGTs was proposed as a tool to reconstruct summer seasonal SSTs in the Chinese coastal seas (Lü et al., 2015; Wei et al., 2020) and the Yellow Sea (Kang et al., 2017). Furthermore, the application of a recent

calibration proposed by Fietz et al. (2020) based on a modification of the ring index, as RI-OH' (Lü et al., 2015), has been shown to generate a realistic SST reconstruction along the western Iberian Margin (Davtian et al., 2021).

A fourth, also more recently developed, organic-based temperature proxy, namely the long-chain diol index (LDI), is based on the relative abundance of C_{28} 1,13-, C_{30} 1,13-, and C_{30} 1,15-alkyl diols (de Bar et al., 2020; Rampen et al., 2012). In globally distributed marine surface sediments, the LDI shows a very good correlation with annual mean SST (de Bar et al., 2020; Rampen et al., 2012). Eustigmatophyte algae are a source of long-chain C_{28}-C_{30} 1,13- and C_{30}-C_{32} 1,15-alkyl diols (hereafter diols) (Balzano et al., 2018; Gelin et al., 1997; Méjanelle et al., 2003; Volkman et al., 1992, 1999), but the distribution of diols in open marine sediments is different from that of cultivated eustigmatophytes, and the biological source of marine 1,13- and 1,15-diols remains therefore uncertain (Balzano et al., 2018; Rampen et al., 2012; Versteegh et al., 1997, 2000). Interestingly, high abundances of C_{32} 1,15-diols are found in the river and estuarine waters but are much lower in open marine environments and can therefore be used as an indicator of freshwater input in the marine environment (de Bar et al., 2016; Lattaud et al., 2017; Lattaud, Kirkel, et al., 2018). *Proboscia* diatoms are the biological source of another group of diols, that is, C_{28}-C_{30} 1,14-diols, being used as indicators of high productivity and upwelling conditions (de Bar et al., 2016; Rampen et al., 2007; Rampen, Willmot, et al., 2014; Sinninghe Damsté et al., 2003). Since the LDI was proposed, various studies have documented the application of the LDI and its limitations for SST reconstruction from the Eocene to the Quaternary in diverse marine settings (e.g., de Bar et al., 2016; de Bar, de Nooijer et al., 2019; de Bar, Dorhout, et al., 2019; Lattaud, Lo, et al., 2018; Lattaud et al., 2019; Lopes dos Santos et al., 2013; Plancq et al., 2015; Rodrigo-Gámiz et al., 2014, 2015; Smith et al., 2020; Wei et al., 2020).

The availability of a variety of organic paleothermometers now allows performing comparative multi-proxy studies. Studies combining SST records obtained by $U^{K'}_{37}$ and TEX^{H}_{86} have, for example, been performed in the Eastern Mediterranean (Castañeda et al., 2010), and subsequent studies in the waters offshore southeastern Australia (Lopes dos Santos et al., 2013), in the Sea of Marmara (Becker et al., 2015), and the NW Pacific (Jonas et al., 2017) also applied the LDI. They often reveal divergences in reconstructed SSTs, which have been attributed to differences in production season or water depth of the source organisms. Davtian et al. (2021) recently combined the $U^{K'}_{37}$, TEX^{H}_{86}, and RI-OH' proxies in three deep sea sediment cores located in a north-south transect along the Iberian Margin for the 160-45 ka BP time period. The RI-OH′ proxy and $U^{K'}_{37}$-derived SSTs clearly revealed the Dansgaard-Oeschger and Heinrich events better than the TEX^{H}_{86}. Hence, multi-proxy approaches in the reconstruction of past climatic changes are a promising development.

In the westernmost Mediterranean, the first biomarker SST proxy records were derived from applications of the $U^{K'}_{37}$ index (Cacho et al., 1999, 2001, 2002; Martrat et al., 2004, 2014). Subsequent studies have also included the TEX^{H}_{86} index, showing comparable $U^{K'}_{37}$- and TEX^{H}_{86}-derived SST records (Castañeda et al., 2010; Grauel et al., 2013; Huguet et al., 2011; Kim et al., 2015; Nieto-Moreno et al., 2013). However, so far only one study has applied the LDI proxy in marine sediments from the westernmost Mediterranean Sea, namely the Alboran Sea, spanning the last 20 kyr (Rodrigo-Gámiz et al., 2014), whereas the novel RI-OH' proxy has not been applied yet. The initial LDI application showed some similarities of the LDI-derived temperatures with those derived using the $U^{K'}_{37}$-proxy (Rodrigo-Gámiz et al., 2014). In this work, we apply for the first time four organic SST proxies ($U^{K'}_{37}$, TEX^{H}_{86}, RI-OH′, and LDI) in a sedimentary record from the Alboran Sea basin, spanning the last 35 kyr to provide new insights into the paleoclimatic and paleoceanographic conditions that led to the rapid climate variability like some D/O cycles and H events. The organic multi-proxy approach is aimed at obtaining robust SST records and constraining potential uncertainties in each proxy, related to calibrations or biasing factors (e.g., depth of habitat, the influence of other biological sources, seasonal productivity). We integrate these data with records of the accumulation rates of different biomarkers used for SST reconstruction, the fractional abundance of C_{32} 1,15-diol, the degree of cyclization of the tetramethylated brGDGTs, the total organic carbon (TOC) content, the stable carbon isotopic composition of organic matter ($\delta^{13}C_{org}$) and the BIT index along the time period recovered. Furthermore, we have compared our multi-SST proxy records with previously obtained climate records from the Alboran Sea (Cacho et al., 1999; Rodrigo-Gámiz et al., 2014).
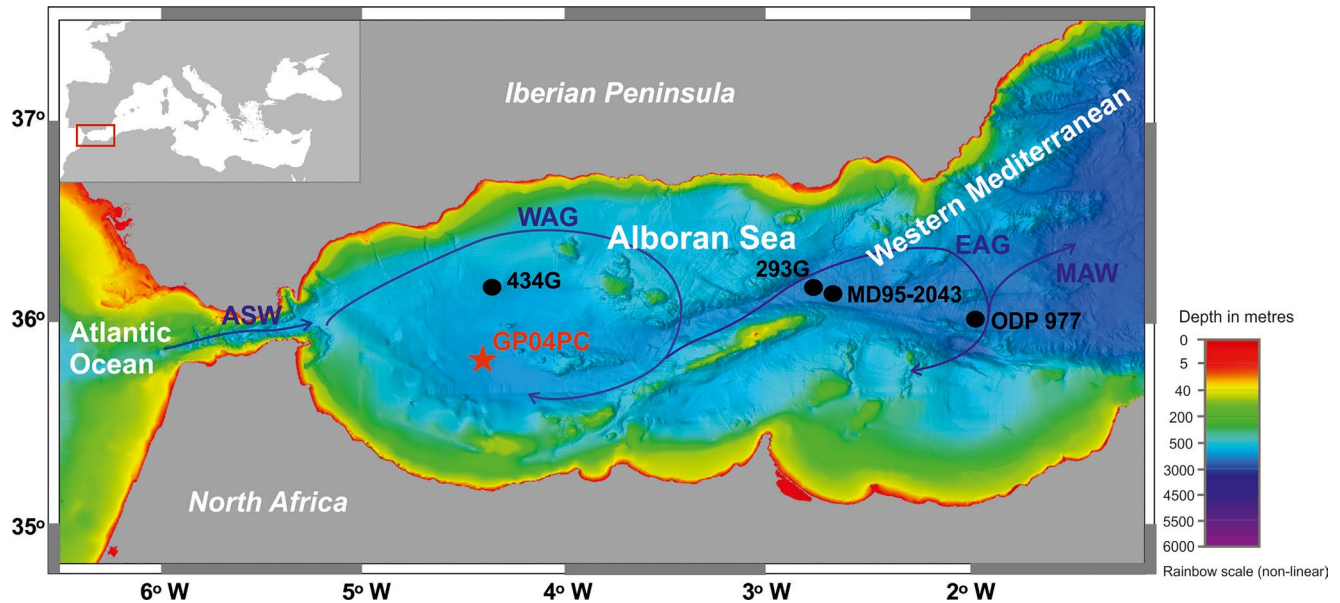
Figure 1. Map with the location of core GP04PC spanning the last 35.2 kyr (red star, this study), core 434G (black circle) spanning the last 14 kyr (Kim et al., 2015; Rodrigo-Gámiz et al., 2014), both located in the western Alboran Sea basin, and core 293G spanning the last 20 kyr (black circle) (Kim et al., 2015; Rodrigo-Gámiz et al., 2011, 2014), core MD95-2043 spanning the last 50 kyr (black circle) (Cacho et al., 1999), and core ODP 977 spanning the last 50 kyr (black circle) (Martrat et al., 2004), all located in the eastern Alboran Sea basin. Bathymetric map from EMODnet Bathymetry website with the depth scale (meters below sea level, mbsl) in form of a non-linear rainbow scale. Blue colors indicate water depths >500 mbsl. Blue arrows represent the theoretical surface circulation in the Alboran Sea. Key: Atlantic surface water (ASW), western Alboran gyre (WAG), eastern Alboran gyre (EAG), and Modified Atlantic Water (MAW).

2. Materials and Methods

2.1. Study Area and Core Sampling

The analyzed record, piston core GP04PC, was recovered in the West Alboran Sea basin, during the oceanographic cruise Gasalb onboard the R/V Pelagia in November 2011 (Figure 1). The coring site (Lat. 35.7871° N, Long. 4.5343° W; water depth 1,306.5 mbsl) is located within the Western Alboran Gyre (WAG) (Fabres et al., 2002; Millot, 1999). The northern edge of the WAG is an upwelling zone characterized by cold waters and high productivity (Sarhan et al., 2000), controlled by seasonal patterns (Sanchez-Vidal et al., 2004). The present-day annual patterns for the WAG, that is, a weaker gyre in winter and a robust gyre during summer and early autumn, is linked to interannual variability of Mediterranean waters, and both probably influence SST (García-Lafuente et al., 2017). At present, the annual mean SST of the westernmost Mediterranean from satellite and modeling data is 19.5 ± 0.3°C; SST ranges from a minimum of 15°C in February to a maximum of 25°C in August (Macias et al., 2016).

After recovery, the core GP04PC (872.25 cm length) was immediately frozen onboard and later on sampled at 1.5 cm intervals. The lithology is dominated by dark-greenish hemipelagic mud-clays with some foraminifera and shell fragments. Samples were split into several fractions for different types of analysis. One of the fractions was kept frozen for biomarker analysis, and another fraction was used to separate planktonic foraminifera for stable isotope analysis and radiocarbon dating.

2.2. Chronology and Stable Oxygen Isotope Stratigraphy

Accelerator mass spectrometry (AMS) ^{14}C dates were determined at the Poznan Radiocarbon Laboratory (Poland) on 10 sediment horizons by picking ca. 10 mg of the planktonic foraminifera *Globigerina bulloides* (size fraction >125 μm). The chronology of the core was obtained using the R-code package rbacon 3.6.2 software (Blaauw & Christen, 2011), using the Marine20 calibration curve (Heaton et al., 2020).

Stable isotope stratigraphy was performed using ca. 10 specimens of *G. bulloides* species (size fraction >125 μm) picked from intervals of 3 cm ($n = 291$; 17 replicate analysis). The oxygen (δ^{18}O) and carbon (δ^{13}C) isotopic

composition of foraminiferal samples were analyzed with an automated Finnigan-MAT Kiel Device Type I, coupled to a Finnigan-MAT 251 mass spectrometer at the Leibniz Laboratory for Radiometric Dating and Stable Isotope Research (Christian Albrechts University of Kiel, Germany). Results were calibrated to the Vienna Pee Dee Belemnite (V-PDB) by means of the NBS-19 carbonate isotope standard and lab standards calibrated. The analytical reproducibility of the instrument was ± 0.07 ‰ for $\delta^{18}O$ and ± 0.04 ‰ for $\delta^{13}C$.

2.3. Bulk Organic Matter Analysis

The total organic carbon (TOC) content and stable carbon isotopic composition of the organic matter ($\delta^{13}C_{org}$) from core GP04PC were obtained for 130 samples and performed at NIOZ. Freeze-dried sediments were acidified with 2N HCl and left overnight to remove carbonates, washed with distilled water to remove acids, and dried overnight in an oven at 60°C. The decalcified sediments were measured in silver foils cup on a Thermo Flash Elemental Analyzer (EA) 1112 coupled via a Conflo II interface to a Thermo Finnigan Delta^{plus} mass spectrometer. The TOC content is reported as the weight percentage of dried sediment (wt. %). The analyses were determined in duplicate and the analytical error was on average <0.2 wt. % for the OC content. The $\delta^{13}C_{org}$ data are reported in the standard delta notation relative to the V-PDB, and were calibrated to a benzoic acid standard ($\delta^{13}C_{org} = -28.1$ ‰ V-PDB calibrated against NBS-22 carbonate isotope standard) and corrected for blank contribution. The analytical reproducibility was usually <0.1 ‰ for the $\delta^{13}C_{org}$.

2.4. Biomarker Extraction and Fractionation

A total of 130 samples were selected from core GP04PC and analyzed at NIOZ. Freeze-dried sediments (ca. 5 g) were homogenized in an agate mortar, mixed with pre-extracted diatomaceous earth, and extracted with an Accelerated Solvent Extractor (Dionex ASE 200), using a solvent mixture of dichloromethane (DCM) and methanol (MeOH) (9:1, *v/v*) at 100°C and 7.6×10^6 Pa. The solvent of the extract was removed in a TurboVap LV Caliper (35°C, 615 mbar or 9 psi), and the total lipid extract (TLE), dissolved in a small amount of DCM, was eluted over a Pasteur pipette column containing Na_2SO_4 using DCM as an eluent and dried again under a stream of N_2. The TLEs were separated by column chromatography into three fractions: apolar, ketone and polar fractions, using a Pasteur pipette column filled with Al_2O_3 (activated for 2 hr at 150°C), eluted with *n*-hexane:DCM (9:1, *v/v*), *n*-hexane:DCM (1:1, *v/v*), and DCM:MeOH (1:1, *v/v*), respectively.

2.5. Alkenone Analysis

For quantitative analysis of alkenones, 1.2 μg of the nonadecane-10-one internal standard (IS) dissolved in 50 μl *n*-hexane was added to the ketone fractions. Analyses were performed with a Gas Chromatography-Flame Ionization Detector (GC-FID; Agilent 6890; equipped with an on-column injector) using a CP Sil-5 fused silica capillary column (50 m; 0.32 mm internal diameter; film thickness of 0.12 μm) and helium as the carrier gas. The oven program was initiated at 70°C and increased by a rate of 20°C per min^{-1} to 200°C and next by a rate of 3°C per min^{-1} until 320°C, maintaining this final temperature for 25 min. Thermo-Atlas software was used for integration of peak areas of the di- and tri-unsaturated C_{37} ketones ($C_{37:2}$ and $C_{37:3}$) and the nonadecane-10-one IS to determine the $U^{K'}_{37}$ index and biomarker concentrations.

The $U^{K'}_{37}$ index was calculated according to the equation formulated by Prahl and Wakeman (1987):

$$U^{K'}_{37} = [C_{37:2}]/([C_{37:2}] + [C_{37:3}]) \tag{1}$$

$U^{K'}_{37}$ values were converted to SST using the global core top calibration ($n = 370$; $r^2 = 0.958$) of Müller et al. (1998):

$$U^{K'}_{37} = 0.033 \times SST + 0.044 \,(r^2 = 0.958, \ n = 370; \ 0 \ m \ \text{water depth}) \tag{2}$$

The calibration error for the $U^{K'}_{37}$ index is 1.5°C (Müller et al., 1998). Duplicate analysis of eight samples showed a mean standard deviation (SD) in the $U^{K'}_{37}$ index of 0.03, equivalent to 1°C.

2.6. GDGT Analysis

For quantitative analysis of GDGTs, 0.01 µg of the C_{46} glycerol trialkyl glycerol tetraether IS (Huguet et al., 2006) was added to an aliquot of the polar fractions dissolved in *n*-hexane:isopropanol (99:1, *v/v*), and filtered using 0.4 µm polytetrafluorethylene filters. Analysis was performed using a High-Performance Liquid Chromatography/Atmospheric Pressure Positive Ion Chemical Ionization-Mass Spectrometry (HPLC/APCI-MS; Agilent Technologies 1110 series equipped with an auto-injector and Chemstation chromatography manager software), according to the methodology described by Hopmans et al. (2016). Identification and quantification of different GDGTs was conducted via single ion monitoring (SIM) of their protonated molecules ([M+H]$^+$) (dwell time of 237 ms per ion) (Figure S1 in Supporting Information S1): *m/z* 1,302.3, 1,300.3, 1,298.3, 1,296.3, 1,292.3, 1,050.0, 1,048.0, 1,046.0, 1,036.0, 1,034.0, 1,032.0, 1,022.0, 1,020.0, 1,018.0, and 743.7 (IS) (Hopmans et al., 2016; Schouten, Huguet, et al., 2007). The OH-GDGTs are dehydrated under APCI conditions resulting in a loss of 18 Daltons, yielding ([M+H]-18)$^+$ ions in the same SIM trace as some of isoGDGTs, that is, *m/z* 1,300.3 for OH-GDGT-0, 1,298.3 for OH-GDGT with one cyclopentane moiety and 1,296.3 for the OH-GDGT with two cyclopentane moieties. The GDGTs identified were manually quantified by integration of their peak areas using MassHunter software.

TEX$^H_{86}$ was calculated according to the GDGT abundances defined by Kim et al. (2010). The numbers (1–3) in Equation 3 correspond to isoprenoid GDGTs from marine Thaumarchaeota with 1-3-cyclopentane moieties, while Cren' is an isomer of Crenarchaeol:

$$\text{TEX}^H_{86} = \log(\text{TEX}_{86}) = \log\left(\,([\text{GDGT-2}] + [\text{GDGT-3}] + [\text{Cren}']) / (\,[\text{GDGT-1}] + [\text{GDGT-2}]\,) + [\text{GDGT-3}] + [\text{Cren}']\,)\,\right) \tag{3}$$

TEX$^H_{86}$ values were transformed into temperatures using the TEX$^H_{86}$ Mediterranean Sea calibration for satellite-derived annual mean SST (Equation 4, Kim et al., 2015):

$$SST = 56.3 \times (TEX^H_{86}) + 30.2\,(r^2 = 0.94,\ n = 45,\ p < 0.001;\ 0\ m\ \text{water depth}) \tag{4}$$

The error for the TEX$^H_{86}$ Mediterranean Sea calibration is 1°C (Kim et al., 2015). Replicate analysis of 41 samples showed a mean SD of 0.008, equivalent to 0.4°C.

The percentage of OH-GDGTs of the total isoGDGTs was calculated according to Huguet et al. (2013):

$$\%\text{OH-GDGT} = ([\Sigma OH\text{-GDGTs}]/([\Sigma OH\text{-GDGTs}] + [\Sigma isoGDGTs])) \times 100 \tag{5}$$

where the OH-GDGTs include OH-GDGT-0, OH-GDGT-1, and OH-GDGT-2, and the isoGDGTs include GDGT-0, GDGT-1, GDGT-2, GDGT-3, Cren and Cren'.

The RI-OH' index was calculated following Lü et al. (2015):

$$\text{RI-OH}' = ([\text{OH-GDGT-1}] + 2 \times [\text{OH-GDGT-2}])/([\text{OH-GDGT-0}] + [\text{OH-GDGT-1}] + [\text{OH-GDGT-2}]) \tag{6}$$

and the SST calibration using the equation proposed by Fietz et al. (2020) was used:

$$SST = (\text{RI-OH}' + 0.029)/0.0422\,(r^2 = 0.76,\ n = 167,\ p < 0.01,\ \text{SD of } 6°C) \tag{7}$$

Replicate analysis of 41 samples showed a mean RI-OH' SD of 0.0095, equivalent to 0.2°C.

The Branched and Isoprenoid Tetraether (BIT) index was calculated following the original definition and equation of Hopmans et al. (2004), slightly modified after Hopmans et al. (2016), including the 5- and 6-methyl isomers of the brGDGTs (de Jonge et al., 2013):

$$\text{BIT} = ([\text{Ia}] + [\text{IIa}] + [\text{IIa}'] + [\text{IIIa}] + [\text{IIIa}'])/([\text{Ia}] + [\text{IIa}] + [\text{IIa}'] + [\text{IIIa}] + [\text{IIIa}'] + [Cren]) \tag{8}$$

where the roman numerals from I-III refer to the predominant brGDGTs without any cyclopentane moieties yielding ([M+H]$^+$) ions with *m/z* 1022 (tetramethylated Ia), 1036 (pentamethylated IIa and IIa') and 1050 (hexamethylated IIIa and IIIa'), and the prime designation indicates the 6-methyl isomers of the brGDGTs (de Jonge et al., 2013). Replicate analysis of 41 samples showed a mean SD of 0.009 of the BIT index.

The degree of cyclization of the tetramethylated brGDGTs was calculated according to Sinninghe Damsté (2016), where a-c refers to the number of cyclopentane moieties (a is 0; b is 1; c is 2):

$$\#rings_{tetra} = ([Ib] + 2 \times [Ic])/([Ia] + [Ib] + [Ic]) \tag{9}$$

2.7. Long-Chain Diol Analysis

For quantitative analysis of long-chain diols, 0.82 μg of the docosane-7,16-diol IS was added to an aliquot of the polar fraction. Fractions were silylated by adding 10 μl of pyridine and 10 μl of N,O-bis(trimethylsilyl)trifluoroacetamide (BSTFA) and heating in an oven at 60°C for 30 min. After cooling (10–20 min), samples were dissolved in 80 μl of ethyl acetate. Long chain diol analyses were performed using an Agilent Gas Chromatograph 7890B (GC) coupled to an Agilent 5977A Series Gas Chromatograph/Mass Selective Detector (GC/MSD). The instrument was equipped with an Agilent CP7740 CP-Sil5-CB fused silica capillary column (25 m; 0.32 mm internal diameter; film thickness of 0.12 μm) using helium as the carrier gas. The GC oven temperature was programmed to start at 70°C, next was increased to 130°C at a rate of 20°C min^{-1}, and then to the final temperature of 320°C at a rate of 4°C min^{-1}, held for 25 min. The internal standard and other diols were quantified using selected ion monitoring (SIM) of the masses m/z 187 (IS), 299, 313, 327, and 341, respectively, and the relevant peak areas were manually integrated using the MassHunter software.

The Long chain Diol Index (LDI) was calculated according to the diol abundances, and transformed into SST, as described by the equations of Rampen et al. (2012) and de Bar et al. (2020), respectively:

$$LDI = [C_{30}\ 1,15 - diol]/([C_{28}\ 1,13 - diol] + [C_{30}\ 1,13 - diol] + [C_{30}\ 1,15 - diol]) \tag{10}$$

$$LDI = 0.0325 \times SST + 0.1082\ \ (n = 514;\ \ r^2 = 0.88) \tag{11}$$

The calibration error for the LDI is 3.0°C (de Bar et al., 2020). Replicate analysis of 11 samples showed a mean SD of 0.019, equivalent to 0.6°C.

3. Results

3.1. Stable Oxygen Isotope Record and Age Model

The δ^{18}O values of the planktonic foraminifera *G. bulloides* varied between a minimum of 0.14 ± 0.07 ‰ at 7.2 kyr and a maximum of 3.44 ± 0.07 ‰ at 17.4 kyr cal. BP (Figure 2a). During the LGM and last deglaciation, the average δ^{18}O value is 2.70 ‰ ± 0.07 ‰, while in the Holocene the average δ^{18}O value is 0.70 ‰ ± 0.07 ‰. The age model of core GP04PC is based on 10 AMS ^{14}C dates determined on picked specimens of *G. bulloides* (Table 1). Furthermore, the chronological control was obtained using six tie-points within the time interval 12–35 kyr (Table 1; Figure 3) from a comparison of the δ^{18}O *G. bulloides* record (Figure 2a) with those of core 293G (Rodrigo-Gámiz et al., 2011) and core MD95-2043 (Cacho et al., 1999) (Figure S2 in Supporting Information S1). These two records come from the eastern Alboran Sea basin (Figure 1) and span the last 20 and 50 kyr, respectively. The age-depth model was developed using a Bayesian statistic of calibrated ages and tie-points (Figure 3) using the R-code package rbacon 3.6.2 software (Blaauw & Christen, 2011) and the Marine20 calibration curve (Heaton et al., 2020). The age model showed that core GP04PC covered the last 35 kyr (specifically last 35,271 years), comprising abrupt climate variations like the D/O interstadials 7-1, the last three H events, the LGM, the B-A and the YD periods. The mean sedimentation rate obtained is 26 cm/kyr, which is comparable with the mean sedimentation rate of core 293G (20 cm/kyr) (Rodrigo-Gámiz et al., 2011), and lower than that of core MD95-2043 (>30 cm/kyr) (Cacho et al., 2002).

3.2. Organic Carbon Content and Biomarker Accumulation Rates and Ratios

The TOC content of core GP04PC ranges from minimum values of 0.40 (at 24.4 kyr cal. BP) to maximum values of 1.13 ± 0.2% (at 8.9 kyr cal. BP) (Figure 4a). Only a few data points in the Holocene interval were analyzed since this period has been previously studied at higher resolution in other Alboran Sea records (Nieto-Moreno et al., 2011; Rodrigo-Gámiz et al., 2011). Enhanced TOC contents were registered in time periods corresponding to the D/O interstadials 7, 6, 5, at the end of H3, H2, and LGM, and from the beginning of H1 and YD to ca. 9 kyr,
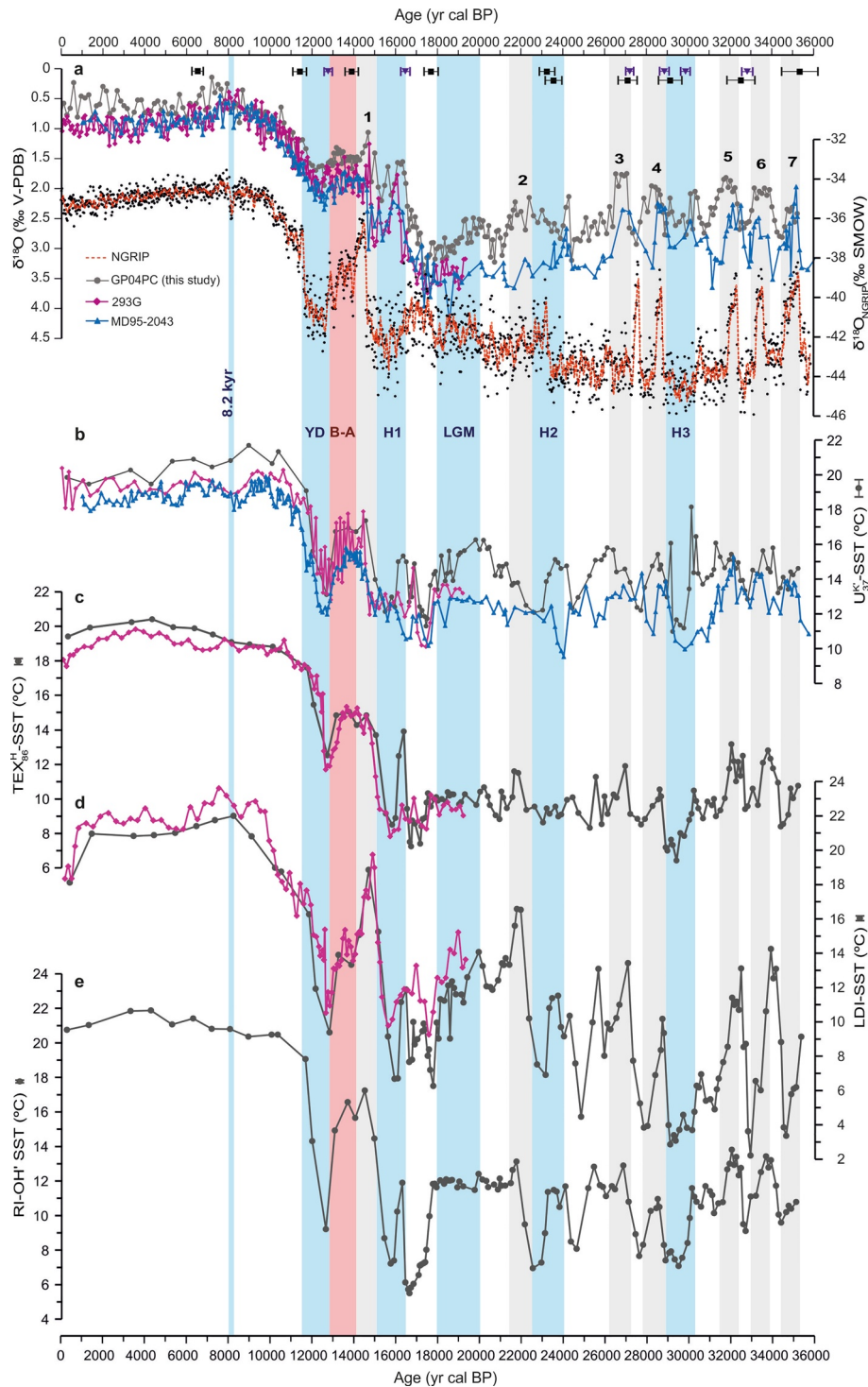
Figure 2.

which corresponds to the time period of the Organic Rich Layer 1 (ORL1) deposition in the Alboran Sea (Cacho et al., 2002; Pérez-Asensio et al., 2020; Rodrigo-Gámiz et al., 2011).

The $\delta^{13}C_{org}$ varies from -21.6 to -25.3 ‰, showing three distinct intervals with more negative $\delta^{13}C_{org}$ values (Figure 5a), that is, during the H2, at the end of the LGM, and at 8.9 kyr, coinciding with some of the maxima in the TOC profile (Figure 4a).

Table 1
Accelator Mass Spectrometry [14]C Carbon Dating of Single Planktonic Foraminifera Globigerina Bulloides (>125 μm) Taken From the Marine Record GP04PC and Tie-Points Used From δ^{18}O Records of Nearby Cores 293G (Rodrigo-Gámiz et al., 2011, 2014) and MD95-2043 (Cacho et al., 1999)

Sample description: Section and interval (cm)	Core depth (cm)	Laboratory code	[14]C AMS age (BP)	Calibrated age (cal. yr BP)[a]
GP04PC_11 (116–117.5)	116.75	Poz-66210	$6{,}210 \pm 35$	$6{,}441 \pm 232$
GP04PC_10 (217–218.5)	217.75	Poz-66209	$10{,}290 \pm 60$	$11{,}431 \pm 340$
Tie-point #1 293G	246.25	–	–	$12{,}690 \pm 70$
GP04PC_09 (320–321.5)	320.75	Poz-66208	$12{,}510 \pm 80$	$13{,}987 \pm 192$
Tie-point #2 293G	362.75	–	–	$16{,}385 \pm 85$
GP04PC_08 (422–423.5)	422.75	Poz-68950	$15{,}160 \pm 90$	$17{,}659 \pm 386$
GP04PC_06 (564.5–566)	565.25	Poz-73151	$18{,}600 \pm 140$	$22{,}230 \pm 491$
GP04PC_05 (572–573.5)	572.75	Poz-96188	$19{,}710 \pm 110$	$22{,}571 \pm 437$
Tie-point #3 MD95-2043	665.75	–	–	$27{,}187 \pm 145$
GP04PC_05 (666.5–668)	667.25	Poz-68948	$21{,}890 \pm 180$	$27{,}171 \pm 456$
Tie-point #4 MD95-2043	689.75	–	–	$28{,}700 \pm 170$
GP04PC_04 (716–717.5)	716.75	Poz-96187	$24{,}960 \pm 170$	$29{,}119 \pm 591$
Tie-point #5 MD95-2043	725.75	–	–	$29{,}794 \pm 195$
GP04PC_03 (808.5–810)	809.25	Poz-96186	$28{,}040 \pm 230$	$32{,}547 \pm 630$
Tie-point #6 MD95-2043	809.25	–	–	$32{,}883 \pm 230$
GP04PC_03 (871.5–873)	872.25	Poz-65478	$31{,}700 \pm 500$	$35{,}241 \pm 976$

[a]Age calibration was calculated using the R-code package rbacon 3.6.2 software (Blaauw & Christen, 2011) and the Marine20 calibration curve (Heaton et al., 2020) at 95% confidence level.

The accumulation rate (AR) of summed $C_{37:3}$ and $C_{37:2}$ alkenones ranges from 0.3 mg/cm^2/yr (24.7 kyr cal. BP) to 47 mg/cm^2/yr (13.1 kyr cal. BP, B-A period) (Figure 4b). High ARs are reached at the D/O interstadials 7 and 5 to 2, and during the B-A period, whereas lower ARs are recorded during the three H events, at the end of the LGM, and progressively decrease during the YD to reach low values during the Holocene. Although the concentration of the $C_{37:4}$ alkenone is low (mean of 3%–4%), a slight increase in the fractional abundance is observed during the three H events, ranging between 10% and 15% (Figure S3 in Supporting Information S1).

GDGTs are the most abundant group of lipids analyzed. The AR of summed isoGDGTs ranges from 17 (at 20 kyr cal. BP) to 580 mg/cm^2/kyr (at 14.1 kyr cal. BP) (Figure 4c). In general, the highest isoGDGT ARs are registered during D/O interstadials 7-3 (especially ca. 28.5 and 27.1 kyr cal. BP), and between 18 and 13 kyr, that is, the period between the end of LGM and the end of the B-A, similar to the TOC profile (Figure 4c). Conversely, lower isoGDGT ARs characterize the Holocene, with the exception of a peak of 169 mg/cm^2/yr at the "8.2 kyr" event. The concentrations of OH-GDGTs are strongly correlated to those of the isoGDGTs (Figure 6a; $r^2 = 0.88$ p-value < 0.001), although the OH-GDGTs typically only represent 2%–3% of those of the isoGDGTs. The AR profile of summed brGDGTs is also similar to that of the isoGDGTs (Figures 4c and 5c). Summed brGDGT ARs

Figure 2. Proxy records from core GP04PC. (a) δ^{18}O record of planktonic foraminifera *G. bulloides* (note the reversed scale), and reconstructed sea surface temperatures (SSTs) using (b) U$^{K'}_{37}$ (C$_{37}$ ketone unsaturation ratio from haptophyte algae; Prahl & Wakeman, 1987), (c) (TetraEther indeX of tetraethers consisting of 86 carbon atoms (TEX$^H_{86}$) from Kim et al., 2010; Thaumarchaeota, Schouten et al., 2002, (d) Long chain Diol Index (LDI) with 28 and 30 carbon atoms and alcohol groups at C$_1$ and C$_{13}$ or C$_{15}$, presumably from eustigmatophytes (Rampen et al., 2012), and (e) RI-OH' (average number of cyclopentane moieties of hydroxy iso; GDGTs; Fietz et al., 2020) proxies. The analytical error associated with the measurement of each biomarker-derived SST is indicated next to each *y*-axis. For reference, the δ^{18}O profile of planktonic foraminifera *G. bulloides* and biomarker-derived SSTs in core 293G (pink, (a)-(d) (Kim et al., 2015; Rodrigo-Gámiz et al., 2014), updated by using a new age model obtained with Bayesian statistics and the Marine20 calibration curve (Blaauw & Christen, 2011; Heaton et al., 2020), the δ^{18}O profile of Greenland NGRIP ice core (data points are black circles and the dashed red line is the 5-points running mean) (Andersen et al., 2006; Svensson et al., 2008) and the δ^{18}O profile of planktonic foraminifera *G. bulloides* in core MD95-2043 (blue, (a) (Cacho et al., 1999). The light blue bars show the main cold events during the last 35.2 kyr, that is, the "8.2 kyr" cold event, the Younger-Dryas, the Last Glacial Maximum, the last three Heinrich events (H1, H2, and H3). The Bölling-Alleröd (b)–(a) event is indicated in a light red bar, and the Dansgaard-Oeschger interstadials (1–7) (Bond et al., 1993; Dansgaard et al., 1993) are in light gray bars. The age model is based on ten ^{14}C accelerator mass spectrometry dates and six tie-points plotted as black and purple symbols, respectively, at the top of the figure.
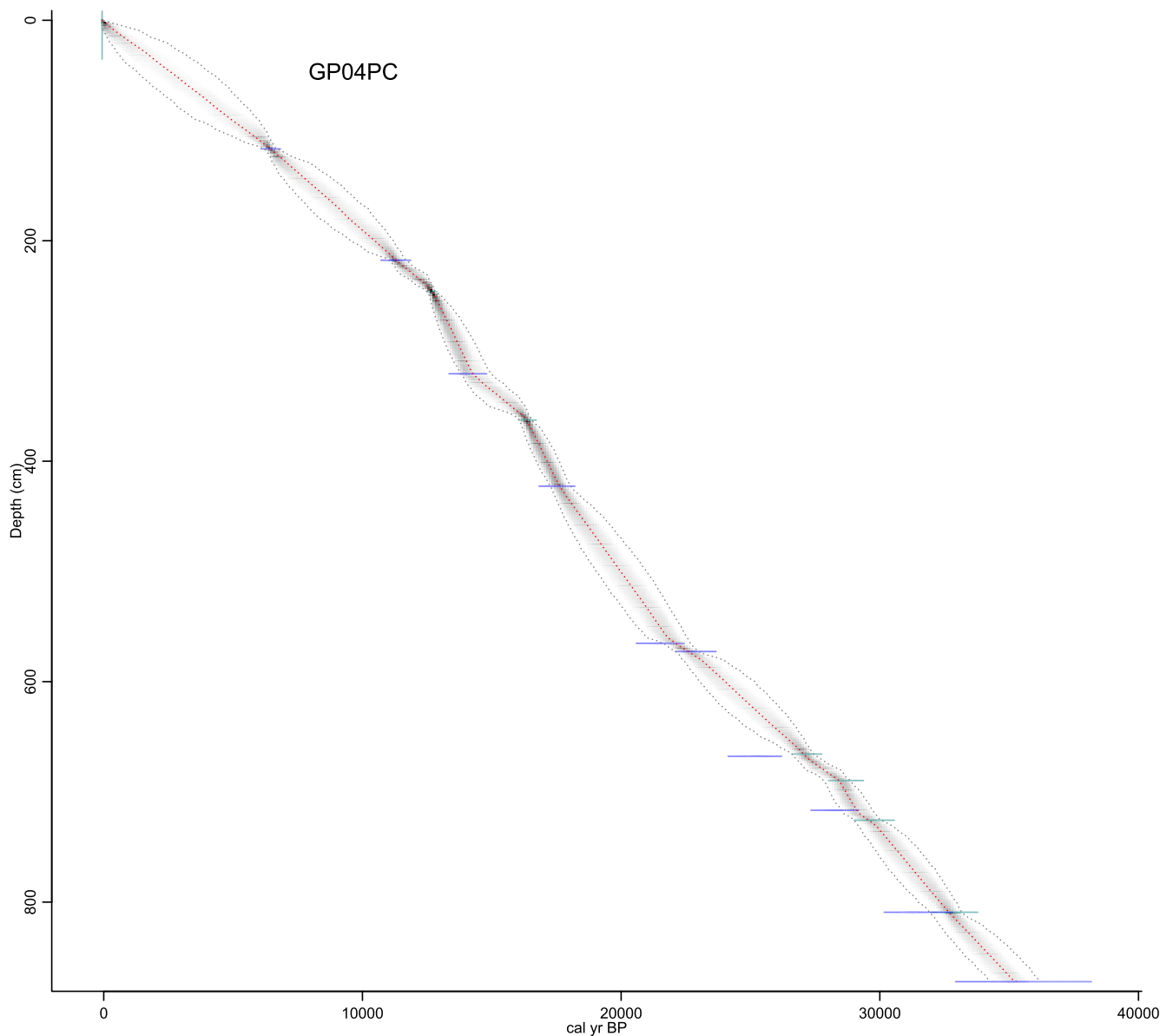
Figure 3. Age-depth model of core GP04PC constructed using ten ^{14}C accelerator mass spectrometry and six tie-points. The purple segments represent the calibrated age ranges corresponding to each radiocarbon date. The green segments represent the adopted tie-points from the $\delta^{18}O$ records of marine cores 293G (Rodrigo-Gámiz et al., 2011, 2014) and MD95-2043 (Cacho et al., 1999). The dotted red line corresponds to the age model developed with a Bayesian statistic using the R-code package rbacon 3.6.2 software (Blaauw & Christen, 2011) and the Marine20 calibration curve (Heaton et al., 2020). The gray shaded area represents the error range in age estimations.

vary from 0.9 (at 20 kyr cal. BP) to 12.5 mg/cm^2/yr (at 14.1 kyr cal. BP) with the highest AR occurring from 17.8 to 13.1 kyr cal. BP (end of the LGM to B-A period) (Figure 5c). At the end of the B-A period (ca. 13 kyr cal. BP), the brGDGTs AR starts to decrease abruptly, reaching lower values during the Holocene. The record of the BIT index (Figure 5b) shows low values (≤ 0.04, indicated with a dashed line) for the D/O interstadials 7-3, the B-A, the YD and the Holocene. For the remaining part of the record, BIT index values are higher, reaching values up to 0.10 at the end of the LGM. For the time period between 35.2 and 26 kyr cal. BP, some cyclicity in the BIT index is evident with minima during the D/O interstadials 7-3, and H3 (Figure 5b).

In general, C$_{30}$ 1,15- and 1,13-diols are the most abundant long chain diols. The ARs of summed C$_{28}$-C$_{30}$ 1,14-diols range from 0.8 (at 17.5 kyr cal. BP) to 50.5 mg/cm^2/yr (at 13.7 and 33 kyr cal. BP) (Figure 4d), while the total 1,13- + 1,15-diols AR varies from 1.8 (at 30.1 kyr cal. BP) to 90 mg/cm^2/yr (at 13.7 kyr cal. BP) (Figure 4e).
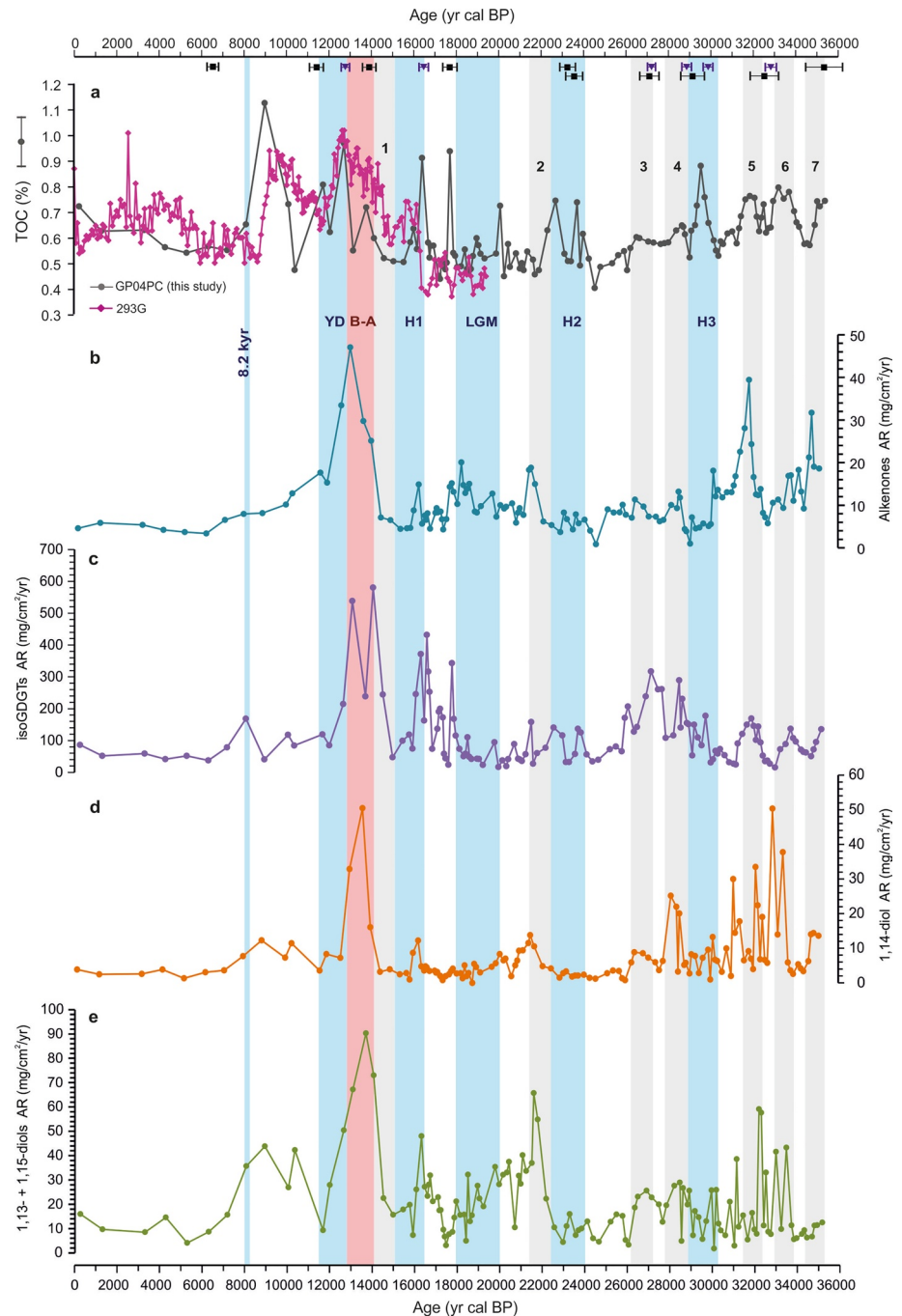
Figure 4. Proxy records from core GP04PC. (a) Total organic carbon content (gray color with the analytical error associated next to y-axis) and data from core 293G (in pink color; Rodrigo-Gámiz et al., 2011). The latter record is plotted after an update of the age model using Bayesian statistic and the Marine20 calibration curve. (b) Accumulation rate (AR) of the $C_{37:2}$ and $C_{37:3}$ alkenones used in the $U^{K'}_{37}$ proxy. (c) ARs of summed isoprenoid glycerol dialkyl glycerol tetraethers. (d) ARs of summed 1,14-diols (produced by *Proboscia* diatoms). (e) AR of the 1,13- + 1,15-diols used in the LDI proxy (i.e., excluding the C_{32} 1,15-diol). The light blue bars show the main cold events during the last 35.2 kyr, that is, the "8.2 kyr" cold event, the Younger-Dryas, the Last Glacial Maximum, the three last Heinrich events (H1, H2, and H3). The Bölling-Alleröd (b)–(a) event is indicated in a light red bar, and the Dansgaard-Oeschger interstadials (1–7) (Bond et al., 1993; Dansgaard et al., 1993) are in light gray bars. The age model is based on ten ^{14}C accelerator mass spectrometry dates and six tie-points plotted as black and purple symbols, respectively, at the top of the figure.
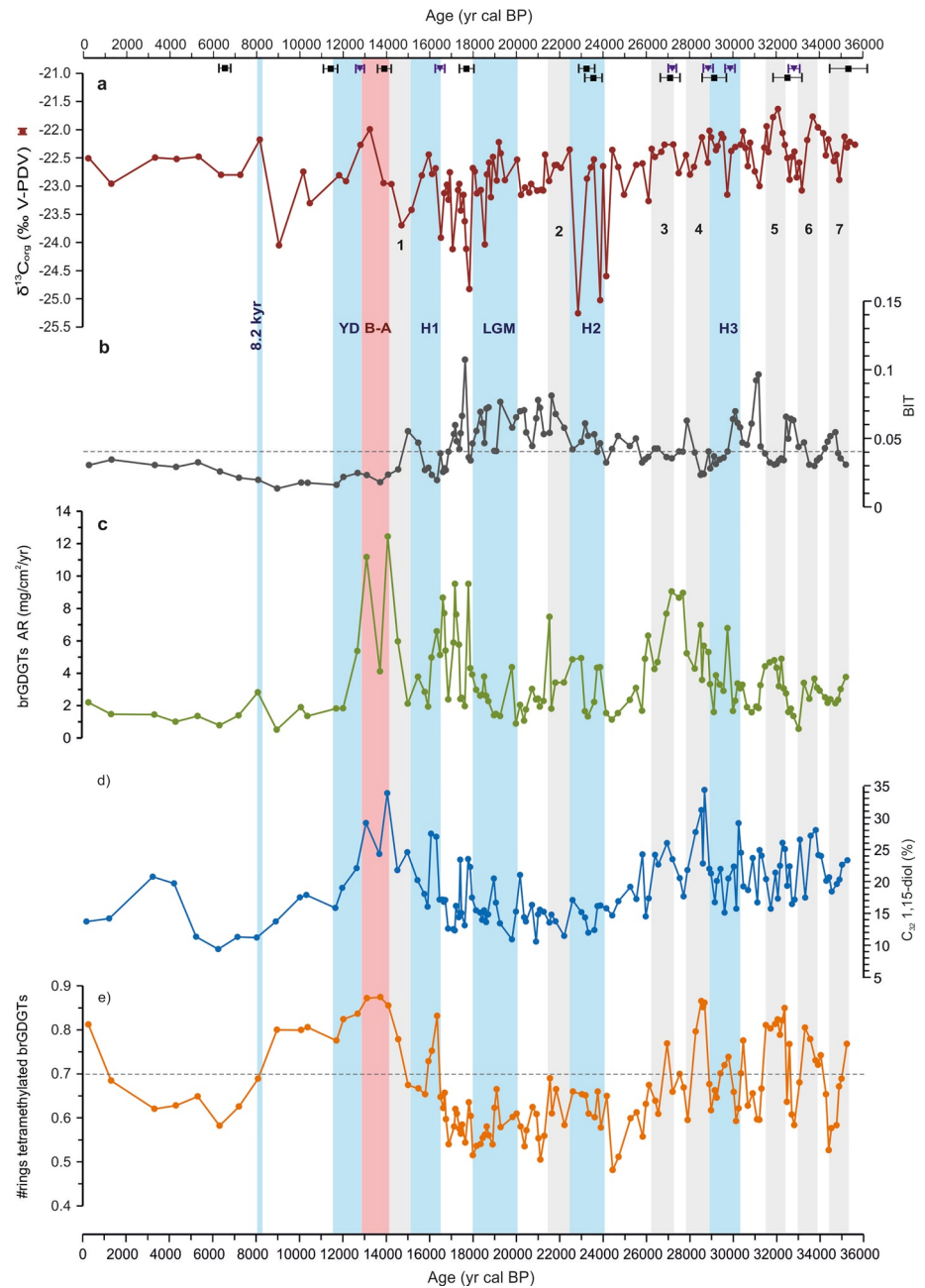
Figure 5. Proxy records from core GP04PC. (a) $\delta^{13}C$ of the bulk sedimentary organic matter with the analytical error associated next to *y*-axis. (b) Branched and isoprenoid tetraether index. (c) Accumulation rate (AR) of summed branched glycerol dialkyl glycerol tetraethers (brGDGTs). (d) The fractional abundance of the C_{32} 1,15-diol with respect to all 1,13- and 1,15-diols. (e) Average number (#rings) of tetramethylated brGDGTs. Color-coded vertical bars indicate warm and cold periods as described in Figure 4.

The summed 1,13- + 1,15-diols AR reveals larger fluctuations than the total 1,14-diols AR, with major values during the D/O interstadials 6-1, the B-A period, and lastly from the beginning of the Holocene to the 8.2 kyr event. The fractional abundance of C_{32} 1,15-diol ranges between 9.5% and 34% of total diols, showing maxima at D/O interstadial 4 (28.5–28.7 kyr cal. PB) and at the beginning of H1 up to the end of the B-A (16.3–13.1 kyr cal. BP) (Figure 5c). The fractional abundance of C_{28} 1,12-diol is generally very low, that is, <0.1% of all diols (data not shown).
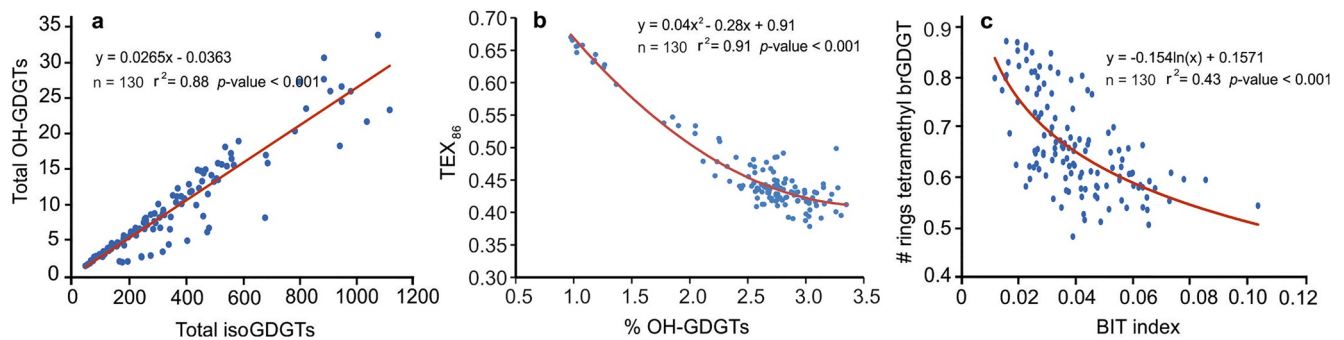
Figure 6. Correlations (red lines) between: (a) Summed concentrations (in μg/g total organic carbon) of isoprenoid glycerol dialkyl glycerol tetraethers (GDGTs) and OH-GDGTs, (b) the fractional abundance of OH-GDGTs (% OH-GDGTs) and TEX$_{86}$, and (c) branched and isoprenoid tetraether index and average number (#rings) of tetramethylated branched GDGTs in core GP04PC.

3.3. Biomarker-Derived SSTs

U$^{K'}_{37}$ derived-SSTs range between 11 and 22°C (Figure 2b). From 35 to 31 kyr cal. BP, SSTs are relatively constant, ca. 13–16°C, followed by a rapid decline at the onset of H3, which recorded the lowest U$^{K'}_{37}$-SSTs of the last 35 kyr (11°C). Low U$^{K'}_{37}$-SSTs are also recorded at the H2 (12°C), at the end of the LGM (17.4 kyr cal. BP, 11°C), at the H1 (12°C), and during the YD (13°C). During the LGM, U$^{K'}_{37}$-SSTs show an average of 15°C, during the B-A of 17°C, and finally the Holocene depicts a period of high SSTs with an average of ca. 20°C (Figure 2b; Table S1 in Supporting Information S1). Application of the Bayesian calibration BAYSPLINE for U$^{K'}_{37}$ (Tierney & Tingley, 2018) results in a similar SST reconstruction with a mean difference of ca. 0.6°C (Figure S4 in Supporting Information S1). Therefore, we have used the Müller et al. (1998) calibration in this study.

Over the whole record, TEX$^{H}_{86}$ derived-SSTs range from 6.4 to 20.4°C (Figure 2c). During D/O cycles 7, 6, and 5 (35-32 kyr cal. BP), SST fluctuate between 8.5 and 13°C, with low SSTs during the stadials (Figure 2c). Lowest TEX$^{H}_{86}$-SST (6.4°C) are reached at H3, ca. 2°C lower than during H2. During the LGM, TEX$^{H}_{86}$-SSTs are relatively constant, ca. 10°C (Figure 2c; Table S1 in Supporting Information S1). A rise in TEX$^{H}_{86}$-SST up to 14°C occurs at the onset of H1, with a minimum SST of 8.5°C. Subsequently, TEX$^{H}_{86}$-SST reaches another minimum at the onset of the YD. The YD-Holocene transition is marked by a sharp TEX$^{H}_{86}$-SST increases of ca. 5°C. SSTs during the Holocene are on average 19°C. We have also examined the Bayesian calibration BAYSPAR for TEX$_{86}$ (Tierney and Tingley, 2014, 2015), resulting in unrealistically high Holocene TEX$_{86}$ absolute temperature values (6-8°C higher than using the Mediterranean calibration by Kim et al. (2015); Figure S5 in Supporting Information S1), and was therefore not considered here.

The RI-OH' SST record shows a similar trend as the TEX$^{H}_{86}$ record, with slightly lower absolute SST values (Figures 2c and 2e). The RI-OH' derived-SST record has minimum values of 5.5°C during the H1 (ca. 16.7 kyr cal. BP) and maxima of 21.9°C during the Holocene (at 4.3 kyr cal. BP) (Figure 2e). The RI-OH' SST record clearly reveals the D/O variability, and reaches low values (5.5–7.5°C) during the H events (Figure 2e). In addition, the relative abundance and distribution of the OH-GDGTs is also clearly related to the distribution of the Thaumarchaeota-derived isoGDGTs used in the TEX$^{H}_{86}$ index (Figures 6a and 6b; $r^2 > 0.8$).

The LDI record shows a SST pattern comparable to that of the U$^{K'}_{37}$, TEX$^{H}_{86}$, and RI-OH' (Figures 2b–2e). The LDI-derived SST record shows, however, the largest temperature range, that is, from 2 to 22°C (Table S1 in Supporting Information S1). Particularly, the D/O interstadials 7 and 6 showed rapid LDI-SST fluctuations, with SST maxima of 13–14°C during interstadials and minima of 2–3°C during the stadials (Figure 2d). Low LDI-derived SSTs values of 3 and 7°C are also recorded during H3 and H2, respectively (Figure 2d). During the LGM, LDI-SSTs varied between 9 and 14°C, with an average of 12°C (Figure 2d; Table S1 in Supporting Information S1). During H1, average LDI-SST was ca. 9°C, which is similar to RI-OH' SST, but 1.4 and 4.8°C lower than the TEX$^{H}_{86}$ and U$^{K'}_{37}$ derived-SSTs, respectively (Table S1 in Supporting Information S1). Subsequently, LDI-derived SSTs increased sharply to ca. 19°C until the beginning of the B-A period, and then abruptly drop again until the YD to ca. 9.5°C (3°C lower than the TEX$^{H}_{86}$-derived SST and similar to RI-OH' derived-SST for this interval). The Holocene LDI-SST average is ca. 20°C; similar to that determined by U$^{K'}_{37}$ and RI-OH', and 1°C higher than the Holocene TEX$^{H}_{86}$-derived SST average (Table S1 in Supporting Information S1).

4. Discussion

4.1. The δ¹⁸O Record: Comparison With Greenland Ice-Core and Nearby Western Mediterranean Records

The stable oxygen isotope ratio of planktonic foraminifera is influenced by changes in SST and salinity, but also depends on ice volume, preservation, and species-dependent vital effects (cf. Urey, 1947; see also Fischer & Wefer, 1999, and references therein). The δ¹⁸O *G. bulloides* record of core GP04PC shows in general the main variations related to D/O cycles as those recorded in the δ¹⁸O NGRIP Greenland ice-record, which mainly reflects air temperature (Andersen et al., 2006; Svensson et al., 2008) (Figure 2a). This reveals the strong link between past climate conditions at high- and mid-latitudes, in agreement with previous studies of δ¹⁸O records from the Alboran Sea (e.g., Cacho et al., 1999, 2002; Martrat et al., 2004; Rodrigo-Gámiz et al., 2011; Sierro et al., 2005). Abrupt shifts to more positive δ¹⁸O *G. bulloides* values are recorded during the main cold climate intervals for the last 35 kyr (Figure 2a). Particularly noticeable are the registered D/O cycles with changes of more than 0.5 ‰ between stadials and interstadials, whereas the expression of the H3, H2, and H1 events is much less pronounced in the δ¹⁸O GP04PC record than in the NGRIP ice-record (Figure 2a). Previous studies of the westernmost Mediterranean comprising the last 250 kyr have also documented different intensities and rates of change in the D/O events with the different marine isotope stages (Martrat et al., 2004). Slightly different patterns in the δ¹⁸O *G. bulloides* record from the GP04PC core with respect to the δ¹⁸O NGRIP ice-record are evident during some D/O interstadials (Figure 2a). In general, the D/O interstadials in the δ¹⁸O GP04PC record are revealed as a more gradual decrease to low stable oxygen isotope values and span ca. 500–600 years, whereas these shifts in the δ¹⁸O NGRIP ice-record are more abrupt and shorter (Figure 2a).

The studied site is under the influence of the western Alboran gyre, and its sedimentary record has been compared with other two marine records, that is, 293G (Rodrigo-Gámiz et al., 2011) and MD95-2043 (Cacho et al., 1999), both located under the influence of the eastern Alboran gyre (Figure 1). Comparison of the δ¹⁸O GP04PC record with those from core 293G for the last 20 kyr shows a similar general trend, with an average offset between the two records of 0.31 ‰ (V-PDB) during the Holocene and 0.44 ‰ (V-PDB) between 15 and 20 kyr cal. BP, with more positive δ¹⁸O values in core 293G than in core GP04PC (Figure 2a). Similarly, a comparison of the δ¹⁸O records of cores GP04PC and MD95-2043 between 20 and 35 kyr cal. BP shows a similar trend with an average offset of 0.49 ‰ (V-PDB), with more positive values of δ¹⁸O in core MD95-2043 (Figure 2a). These offsets within the two Alboran basins may be explained by an intensification of the cold North Atlantic freshwater influx signal due to the eastern Alboran gyre (Rodrigo-Gámiz et al., 2011, 2014), and/or consequent slight changes in salinity. In fact, the high sensitivity of the δ¹⁸O record in the Alboran Sea and the effect of slight variations in salinity and/or temperature have been also previously described during Heinrich events (H) with a marked negative δ¹⁸O *G. bulloides* excursion as a consequence of the incursion of δ¹⁸O depleted meltwaters and low Atlantic seawater salinity (Cacho et al., 2002; Rodrigo-Gámiz et al., 2011; Sierro et al., 2005).

Additionally, a lead response of the δ¹⁸O record to the Bond cycles (with a periodicity of ca. 1,500 years), in the eastern Alboran Sea for the last 20 kyr has been previously described (Rodrigo-Gámiz et al., 2014; 2018). The planktonic foraminifera δ¹⁸O signal was either out of phase or did not correlate at all in the cross-spectral analysis with any of the other paleoenvironmental proxies used, suggesting that the δ¹⁸O record also registered changes in the regional hydrological cycle and not only the global ice volume and temperature (Rodrigo-Gámiz et al., 2018).

4.2. Organic Matter Input: Biomarker Distributions and Productivity

The TOC content in core GP04PC shows some variation over the last 35 kyr (Figure 4a), with maxima recorded during D/O interstadials 7-5, at the end of H3, H2, and the LGM, at the beginning of H1 and the B-A, from where the TOC content starts to be higher up to the Holocene, ca. 9 kyr cal. BP (Figure 4a; gray line). This latter period was previously designated as the ORL1 in marine records from the Alboran Sea with a TOC content of over 0.8% (e.g., Cacho et al., 2002; Rodrigo-Gámiz et al., 2011), and it is more clearly revealed in the high-resolution record of core 293G (Rodrigo-Gámiz et al., 2011) (Figure 4a). The δ¹³C$_{org}$ profile shows some variability that, to some extent, follows the record of the TOC content (Figure 5a). Lower δ¹³C$_{org}$ values up to −25.3‰ occur at the end of the H2 and LGM and ca. 8.9 kyr cal. BP coincides with the end of the ORL1 (Figures 4a and 5a). This could mark an increased influx of terrestrial organic matter (OM), which is depleted in δ¹³C$_{org}$. Indeed, the spike at the end of the LGM coincides with relatively high BIT index values (Figure 5b), which could reveal an increased input of

fluvially-derived terrestrial OM (Hopmans et al., 2004; Ménot et al., 2006; Walsh et al., 2008). The BIT values show a low but significant correlation with the average number of rings tetramethylated brGDGTs (as expressed by the #rings$_{tetra}$ index) (n = 130, r^2 = 0.43, p-value < 0.001; Figure 6c). At low BIT index values, #rings$_{tetra}$ shows values close to those characteristics for in-situ marine production (>0.7) (Figure 6c), while at higher BIT index values (>0.04), #rings$_{tetra}$ is dropping toward levels that are indicative of mixed terrestrial and marine origin (Sinninghe Damsté, 2016) (Figures 5b and 5e, dashed lines show cut-off values). Hence, only at BIT values >0.04 there is evidence for a (partial) terrigenous source of brGDGTs. However, for the other negative excursions in the $\delta^{13}C_{org}$ record, no increased BIT values are observed (Figures 5a and 5b). These excursions also do not coincide with the maxima recorded in the summed brGDGTs AR profile (Figure 5c), suggesting that fluvially-transported continental OM input is not playing a substantial role in the studied marine site. Another indicator of fluvially transported riverine OM input is the % C$_{32}$ 1,15-diol (Lattaud et al., 2017). The fractional abundance of the C$_{32}$ 1,15-diol is always <34%, varying in general from 10%–30% (Figure 5d), which is in range with typical % C$_{32}$ 1,15-diol values for open marine settings (Lattaud et al., 2017; Rampen, Datema, et al., 2014). Some of the increases follow the increases in the brGDGTs AR, but the negative $\delta^{13}C_{org}$ excursions in the Holocene are not recorded in the % C$_{32}$ 1,15-diol, suggesting no major terrestrial OM influence.

Alternatively, the slightly higher TOC content in some parts of the section may be linked to an increase in productivity and/or preservation conditions. Previous studies of the Alboran Sea sedimentary record have suggested enhanced primary productivity during the D/O interstadials and other warm periods, which may have been caused by increased levels of nutrients by fluvial input or wind-induced upwelling (e.g., Ausín et al., 2015; Colmenero-Hidalgo et al., 2004; Incarbona et al., 2013; Moreno et al., 2004). Our data set provides productivity markers in the form of ARs of biomarkers for three groups of primary producers (i.e., haptophytes, diatoms, and eustigmatophyte algae). This is all under the assumption that conditions for biomarker preservation in the sediments (i.e., primarily determined by bottom water oxygen concentrations) remained constant as this may affect biomarker concentrations and ARs differently (Sinninghe Damsté, Rijpstra, & Reichart, 2002).

The record of alkenone AR may be interpreted as a production record of haptophyte algae (including coccolithophorids). High alkenone ARs are recorded during D/O interstadials 7, 5, and during the B-A period (Figure 4b). High concentrations of C$_{37}$ alkenones in sediments deposited during the B-A period and early Holocene have previously been related to progressively humid conditions and concomitant nutrient input by a fluvial discharge that also led to a stratified upper water column (e.g., Ausín et al., 2015; Cacho et al., 2002; Pérez-Asensio et al., 2020; Rodrigo-Gámiz et al., 2011), explaining the high content and good preservation of OM that characterizes the ORL1 deposition in the western Mediterranean. *Proboscia* diatoms are the predominant source of C$_{28-30}$ 1,14-diols and these biomarkers have been shown to be useful indicators of *Proboscia* productivity increases in upwelling areas (Rampen et al., 2007; Sinninghe Damsté et al., 2003). Particularly in the western Alboran Sea basin, strong upwelling conditions have been described during the spring and summer seasons (Sanchez-Vidal et al., 2004). In the studied record, their ARs clearly peak in the first part of the record, that is, 33.5–31.2 kyr cal. BP, suggesting that the upwelling was less intense during stadials and more intense during interstadials, as is also shown by the alkenone ARs (Figures 4b and 4d). Furthermore, the algae producing the C$_{28-30}$ 1,13- and 1,15-diols, possibly eustigmatophytes, might occur in the summer season (Rampen et al., 2012). Their ARs show substantial variation along the record with higher values in most of the D/O interstadials and the B-A period and from the early Holocene to the end of the ORL1 (Figure 4e).

Thaumarchaeotal-derived isoGDGTs were the most abundant lipids recorded for the last 35.2 kyr with ARs up to 580 mg/cm^2/yr, higher than those of the diols (total diol ARs up to 170 mg/cm^2/yr) and alkenones (AR up to 47 mg/cm^2/yr). Thaumarchaeota are nitrifiers (Könneke et al., 2005; Wuchter et al., 2006) and rely for their ammonium primarily on the breakdown of freshly produced OM by phytoplankton. ARs of isoGDGTs are higher in the glacial than in the Holocene but also vary markedly showing a major increase during D/O 7-3 and from the end of the LGM to the end of the B-A (Figure 4c), as shown for primary productivity biomarkers.

4.3. Comparison of the Biomarker-Derived SST Records (U$^{K'}_{37}$, TEX$^H_{86}$, RI-OH', and LDI)

The four organic temperature proxies reveal a similar general SST trend over the last 35 kyr, although with substantial variations in their absolute values (Figures 2b–2e, Figure S6 in Supporting Information S1). Cross-plots between the SSTs reconstructed by the different proxies show the highest correlation for TEX$^H_{86}$ and RI-OH' (Figure 7e, n = 130, r^2 = 0.86, p-value < 0.001), followed by U$^{K'}_{37}$ and RI-OH' (Figure 7c, n = 130, r^2 = 0.77,
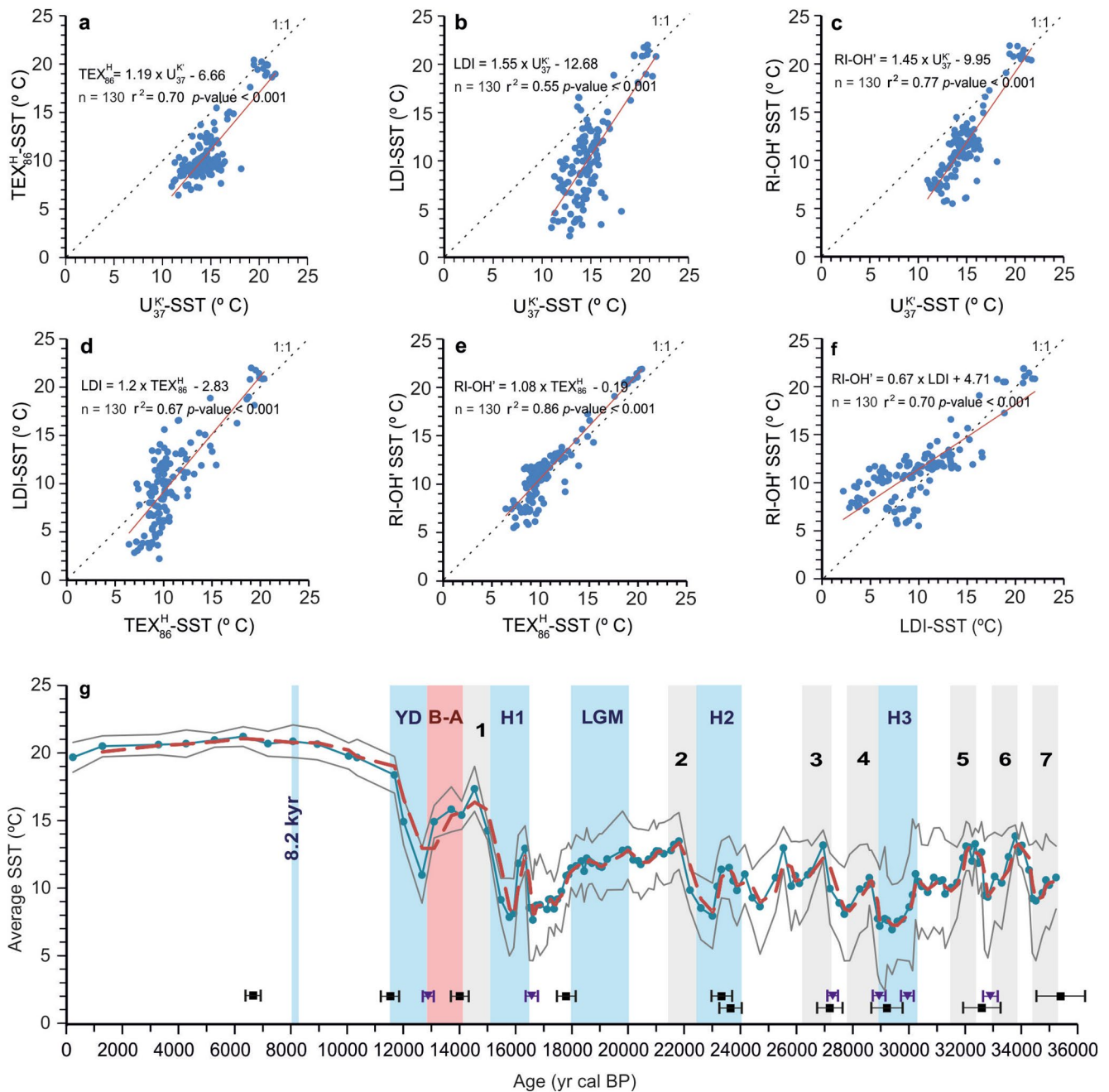
Figure 7. Correlations between sea surface temperatures (SST) estimated using the four independent organic paleothermometers in core GP04PC during the last 35.2 kyr: (a) $U^{K'}_{37}$ and TEX^H_{86}, (b) $U^{K'}_{37}$ and long chain diol index (LDI), (c) $U^{K'}_{37}$ and RI-OH', (d) TEX^H_{86} and LDI, (e) TEX^H_{86} and RI-OH', and (f) LDI and RI-OH'. The red line shows the linear correlation; the 1:1 line is provided as reference. (g) Age-profile of the average organic proxy-derived SST record integrating the four organic proxies ($U^{K'}_{37}$, TEX^H_{86}, RI-OH' and LDI). Gray lines indicate the standard deviation (+SD and -SD) of the four proxy-SST estimations. Red dashed line shows the 2-points running mean.

p-value < 0.001), and then by $U^{K'}_{37}$ and TEX^H_{86} (Figure 7a, $n = 130$, $r^2 = 0.70$, p-value < 0.001). A high, albeit slightly lower ($r^2 = 0.59$), correlation of $U^{K'}_{37}$- and TEX^H_{86}-derived SSTs has previously been observed in the western Mediterranean for the penultimate interglacial-to-glacial cycle (Huguet et al., 2011). The correlation between $U^{K'}_{37}$- and LDI-derived SST is less developed but still significant (Figure 7b, $n = 130$, $r^2 = 0.55$, p-value < 0.001). LDI- and TEX^H_{86}-derived SSTs are also well correlated (Figure 7d, $n = 130$, $r^2 = 0.67$, p-value < 0.001). Furthermore, derived-SSTs are in good agreement with previous $U^{K'}_{37}$-, TEX^H_{86}- and LDI-derived

SST records from the Alboran Sea previously determined for the last 20 kyr (Figures 2b–2d) (Kim et al., 2015; Rodrigo-Gámiz et al., 2011).

In terms of absolute values, TEX^H_{86}-, RI-OH'- and LDI-derived-SSTs are lower than $U^{K'}_{37}$-derived SSTs from 35 to 8.9 kyr cal. BP, while for the remaining part of the record (8.9 kyr cal. BP-present), TEX^H_{86}-SSTs are slightly lower and RI-OH'- and LDI-derived SST are higher (Figures 2b–2e; Figure S6 in Supporting Information S1). The RI-OH'-derived SST record follows a similar trend as the TEX^H_{86}-derived profile, although with lower absolute temperature values from the end of the LGM to the YD, in agreement with the LDI profile (Figures 2b–2e; Figure S6 in Supporting Information S1). $U^{K'}_{37}$-derived SSTs reveals minor scale variation compared to the other three SST records, while the LDI-derived SST record presents the widest range. The differences in estimated SSTs are larger before the LGM, especially between 24.7 and 35.2 kyr (Figures 2b–2e; Figure S6; Table S1 in Supporting Information S1), where $U^{K'}_{37}$- and LDI-derived SSTs show the highest average offset (6.0°C), while the average offset between $U^{K'}_{37}$-, RI-OH'- and TEX^H_{86}-derived SSTs is smaller (3.3–4.2°C). The LDI derived-SST record and, to a lesser extent, the TEX^H_{86}- and RI-OH'- derived-SST records reveal abrupt climate events, such as the D/O (inter)stadials from 35.2-26 kyr cal. BP, in a much more pronounced way than the $U^{K'}_{37}$-derived SST record (Figures 2b–2e and 8b–8e).

Although the analytical errors for these proxies are relatively small, their calibration errors are substantial, that is, 1.5°C for $U^{K'}_{37}$ (Müller et al., 1998), 1.0°C for TEX^H_{86} (Kim et al., 2015), 3.0°C for LDI (de Bar et al., 2020), and, especially, 6°C for RI-OH' (Fietz et al., 2020). The large calibration error for RI-OH' may be due to the so far limited core top calibration and perhaps to non-thermal effects on the OH-GDGTs distribution (Davtian et al., 2021). Hence, the differences in the absolute values of the proxy-derived SST estimates for the Holocene may be statistically insignificant, as discussed earlier for the differences of $U^{K'}_{37}$- and LDI-derived SST estimates obtained in core 434G from the western Alboran Sea (Rodrigo-Gámiz et al., 2014). Moreover, the mean SST difference of 4.5°C is larger than the standard error of 0.3°C calculated according to Davtian et al. (2019), that is, $\sqrt{[(\text{calibration error } U^{K'}_{37})^2 + (\text{calibration error LDI})^2]}/\sqrt{n}$, indicating that the SST differences are significant and systematically different. Furthermore, the divergence in SST estimated using different organic proxies may also be due to differences or shifts in the growing season of the different biological sources, that is, haptophytes, Thaumarchaeota, and eustigmatophytes, or depth habitat during the deglaciation and glacial periods at different marine settings (i.e., Becker et al., 2015; Castañeda et al., 2010; Davtian et al., 2021; Huguet et al., 2011; Jonas et al., 2017; Lopes dos Santos et al., 2013).

Previous work has shown that $U^{K'}_{37}$-derived temperatures might reflect annual mean SST for the upper 40 m in the Mediterranean (e.g., Cacho et al., 2002; Huguet et al., 2011; Martrat et al., 2004). Nevertheless, $U^{K'}_{37}$-derived temperatures applying the Mediterranean calibration proposed by Ternois et al. (1997) were close to those of summer in the northern Mediterranean (Cacho et al., 2002), while the fluxes of alkenone-producing haptophytes in the Alboran Sea showed maximum values in May during the annual cycle 1997–1998 (Bárcena et al., 2004). $U^{K'}_{37}$-derived SSTs show in general slightly higher temperature values along the last 35 kyr than those obtained in other Alboran marine records, that is, core 293G, MD95-2043, and ODP 977 from the eastern Alboran Sea basin (Figure 1; Figure S5 in Supporting Information S1) (Cacho et al., 1999; Martrat et al., 2004; Rodrigo-Gámiz et al., 2014), and particularly from 35-20 kyr and during the Holocene time periods (Figure 2b). This may be explained by a difference in the haptophyte blooming seasons between the western and eastern Alboran Sea basins, in agreement with the seasonal eastward cooling of surface Atlantic waters during autumn and spring triggered by the oceanographic gyres in the Alboran Sea (e.g., García-Lafuente et al., 2017).

The TEX^H_{86}-derived SST record presents, particularly during the last glacial period (35-17 kyr cal. BP), lower values than the $U^{K'}_{37}$-derived SST record (Figures 2b and 2c; Figure S6 in Supporting Information S1). This may be attributed to variations in the contribution of deep-water dwelling Thaumarchaeota to the sedimentary isoG-DGTs lipid pool. A recent study of the archeal diversity in the Mediterranean water column has demonstrated that Thaumarchaeota dominated in subsurface waters and exhibited a different isoGDGT distribution (Besseling et al., 2019). Therefore, a change in the niche of the Thaumarchaeota during the glacial period in the Alboran Sea may partially explain the larger observed SST range between $U^{K'}_{37}$- and TEX^H_{86}-derived estimations, as has been suggested previously for other marine settings (Becker et al., 2015; Huguet et al., 2011; Jonas et al., 2017). Interestingly, however, despite the strong water depth dependence in the distribution of isoGDGTs involved in the TEX^H_{86} recorded in the sedimentary signal from the Mediterranean Sea, the strongest correlation of TEX^H_{86} values in surface sediments at >1,000 m still is with annual mean SST (Kim et al., 2015) and the specific TEX^H_{86}
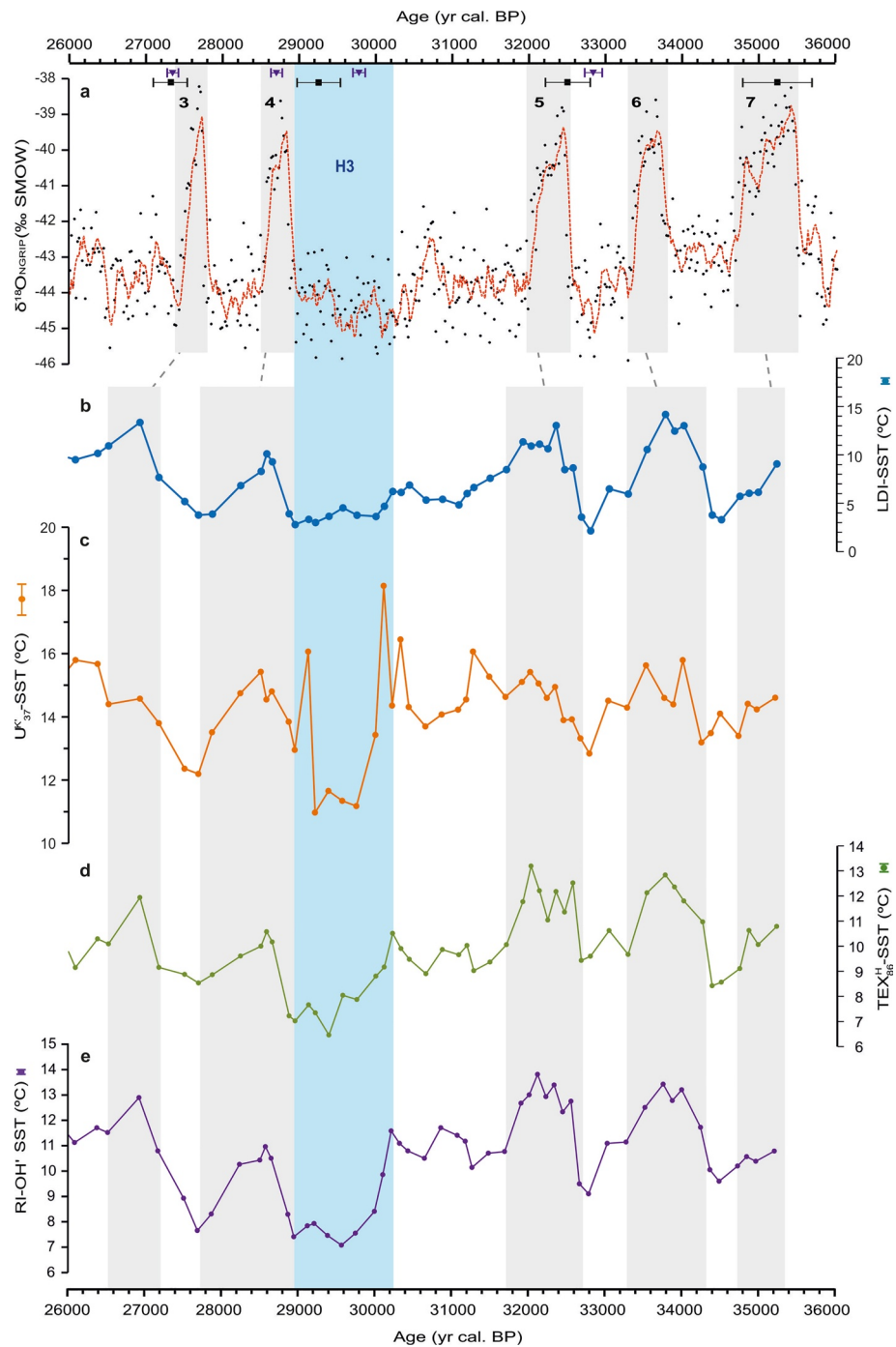
Figure 8. Temperature proxy records from core GP04PC for the time interval between 26 and 35.2 kyr in comparison with Greenland ice core data. (a) δ^{18}O profile of Greenland NGRIP ice core (data points are black circles and the dashed red line is the 5-points running mean) (Andersen et al., 2006; Svensson et al., 2008). (b) LDI-SST. (c) $U^{K'}_{37}$-SST. (d) TEX^{H}_{86}-SST, and (e) RI-OH' SST. The analytical error associated with the measurement of each biomarker-derived SST is indicated next to each y-axis. Blue bar indicates the Heinrich event 3 (H3), and gray bars indicate the Dansgaard-Oeschger (D/O) interstadials (3–7) (Bond et al., 1993; Dansgaard et al., 1993). [14]C Accelerator mass spectrometry dates and tie-points used for the age model are plotted as black and purple symbols, respectively, at the top of the figure.

-SST calibration applied here takes the contribution of the deep water-dwelling Thaumarchaeota into account. The good correlation of RI-OH'- and TEX$^H_{86}$- derived SSTs together with the general match in absolute values (Figure 7e) is in line with their common origin from Thaumarchaeota and supports a response to growth temperature in the Thaumarchaeotal lipid composition. This is further supported by the correlation of the absolute abundance of isoGDGTs and OH-GDGTs (Figure 6a) and the clear inverse correlation of the abundance of OH-GDGTs and TEX$_{86}$ (Figure 6b). This relationship between the distribution of OH-GDGTs and SSTs has also been observed at middle- and low-latitude marine areas with low terrigenous inputs (Fietz et al., 2013; Huguet et al., 2013; Kaiser & Arz, 2016), as well as in a marginal basin in the western Mediterranean with substantial terrigenous input (Davtian et al., 2019), confirming their potential use as paleotemperature proxy. Although other studies have proposed a different thermal response of archeal OH-GDGTs at settings with temperatures >25°C (Yang et al., 2018) or in waters below 200 m (Wei et al., 2020) in the South China Sea, such deviations are not evident from the work presented here.

The LDI-derived SST record showed minima at D/O stadials 6, 5, and 3, during the three H events and the YD (Figure 2d; Figure S6 in Supporting Information S1). Both the original and recently updated global LDI calibrations using surface sediments show the best correlation with summer/autumn SST for the upper 30 m surface waters (de Bar et al., 2020; Rampen et al., 2012). Assuming a niche in the surface water for diol-producers, these reconstructed SST minima in the glacial period seem unrealistically low (i.e., down to 2°C) for the westernmost Mediterranean. Under certain circumstances, the LDI proxy is not reliable, that is, when long-chain diol distributions are dominated by 1,14-diols produced by *Proboscia* diatoms, which also produce traces of C$_{30}$ 1,13-diol and C$_{28}$ 1,12-diol (de Bar et al., 2020; Rampen et al., 2012). This may influence the distribution of diols produced by eustigmatophyte algae and hence LDI values. High concentrations of 1,14-diols are recorded from 33.5-31.2 kyr cal. BP covering the D/O 6, during the D/O interstadial 4, and during the B-A (Figure 4d), indicating periods of enhanced productivity of *Proboscia* diatoms. This may have had an influence by decreasing the LDI-reconstructed SSTs as has been documented in other marine settings (de Bar et al., 2020; Rampen et al., 2012). The average contribution of 1,14-diols to total diols is slightly >30% in the range between 27.7 and 35 kyr cal. BP, with in some cases reaching 54%. Nevertheless, it has recently been shown that a fractional abundance of the C$_{28}$ 1,12-diol > 0.1 is a better indication for the influence of *Proboscia* species on the LDI than the abundance of 1,14-diols (de Bar et al., 2020). The contribution of the C$_{28}$ 1,12-diol is low (<0.1 with a mean < 0.03) in our studied record, suggesting that interference by *Proboscia* diatoms is not a proper explanation for the low LDI-reconstructed SSTs. Another explanation for the low SST values during the glacial period may be freshwater input that can influence in-situ produced marine diol distribution (de Bar et al., 2016; Lattaud et al., 2017; Lattaud, Kirkel, et al., 2018). This can be easily monitored by determining the fractional abundance of the C$_{32}$ 1,15-diol, a dominant diol in freshwater eustigmatophyte algae, of all 1,13- and 1,15-diols; this varies between 10%–34% (Figure 5d), with an average value of 19%. In the surface sediment set studied by Rampen et al. (2012), the C$_{32}$ 1,15-diol abundance does not exceed 20%. Hence, the lower LDI-SST values may be related to higher abundances C$_{32}$ 1,15-diol, although in general, the fractional abundance of C$_{32}$ 1,15-diol does not exceed the common values for marine surface sediments. In principle, other environmental factors influencing the LDI proxy and biasing derived temperatures like nutrient availability or changes in salinity or oxygen in the western Mediterranean can be discarded (Rampen et al., 2012). Nevertheless, further work on the marine water column is required to better understand the distributions of the diol-producers and the production season along the year in this region.

In general, differences between absolute SSTs reconstructed using inorganic and organic proxies have been previously observed at different marine core sites in the Mediterranean, Atlantic, Pacific, or Southern Ocean (e.g., Jiménez-Amat & Zahn, 2015; Lopes dos Santos et al., 2013; Magill et al., 2018; Smith et al., 2013). Particularly, besides ecological behavior in the biological sources such as seasonality or depth habitat, differences between derived-SSTs from *G. bulloides* and other organic-based proxies from the same sediment layer could be related to sorting processes, sediment mobilization, or aggregation, among others, but its evidence in the sedimentary record is difficult to resolve (Magill et al., 2018).

4.4. Short-Term Rapid Climate Transitions in the Alboran Sea During D/O Cycles 7-3

The temperature evolution over the last 35 kyr is marked by abrupt and rapid shifts from the glacial period to the last deglaciation, in particular for the period between 35.2 and 26 kyr that includes the D/O cycles 7-3 (Figures 2 and 8). Although the resolution of our SST records is lower than that of the δ^{18}O NGRIP record (Andersen

et al., 2006; Svensson et al., 2008), fine details in the D/O cycles 7-3 (e.g., the absolute minimum in the D/O 6 stadial) are well identified (Figures 2 and 8), especially in the TEX^H_{86}, RI-OH' and LDI derived-SST records. The slight timing differences in age and duration of the D/O interstadials between the NGRIP $\delta^{18}O$ record and the SST records may be related to the uncertainties of the age model, but may also be due to a longer duration of the inter-stadials in the western Mediterranean area. Nevertheless, there is a remarkably good correspondence of the $\delta^{18}O$ NGRIP Greenland ice-record with the LDI-SST record (Figures 8a and 8b). As discussed in the previous section, the magnitude of SST changes revealed by the LDI (ca. 12.2°C for D/O 6) seems unrealistic, but the timing of the SST changes is supported by other organic paleothermometers; the TEX^H_{86} and the RI-OH' derived-SST records also reveal maxima and minima D/O variability, coinciding with those in the LDI-SST record, although the magnitude of change is lower (ca. 3.4°C for TEX^H_{86}-SST and ca. 4.3°C for RI-OH' SST) (Figures 8b, 8d and 8e). The $U^{K'}_{37}$-SST record also shows the maxima and minima but the correlation with the $\delta^{18}O$ NGRIP record is less clear (Figure 8c). An explanation might be related to the different resistance toward oxygen exposure in the sediment of different biomarkers (Sinninghe Damsté, Rijpstra, & Reichart, 2002). It is known that alkenones are more resistant to oxygen exposure than long-chain diols and GDGTs and can thus be transported over longer distances via lateral transport (e.g., Kim et al., 2009; Mollenhauer et al., 2007; Ohkouchi et al., 2002). This may perhaps explain why the $U^{K'}_{37}$-SST shows a less distinct record than the other organic-paleothermometers used. Nevertheless, a similar variability is observed when compared with the $U^{K'}_{37}$-SST record from core MD95-2043 (Cacho et al., 1999) and ODP 977 (Martrat et al., 2004), although with a difference in absolute SST shift as discussed previously (Figure 2b; Figure S3 in Supporting Information S1).

The D/O cycles are also clearly reflected by other biomarker parameters (Figure 9). Total isoGDGTs, and to a lesser extent 1,13- and 1,15-diols, and alkenone ARs (Figures 9b–9d), show maxima at D/O interstadials, suggesting increased marine productivity. The #rings$_{tetra}$ index displays a maximum at each interstadial (Figure 9e), indicating that at these times in-situ production of #rings$_{tetra}$ brGDGTs was dominant over the delivery of brGDGTs from other sources (Sinninghe Damsté, 2016). Accordingly, the BIT index shows the lowest values (0.03–0.04) during the interstadials and the $\delta^{13}C_{org}$ values show positive excursions, although the brGDGTs AR at the interstadials was slightly higher (Figures 5a–5c and 9f). Earlier work in the North Atlantic has noted that the correlation of $\delta^{13}C_{org}$, BIT, and brGDGT concentrations may be explained by changing supplies of continental OM transported by ice rafting debris (IRD) during H-events (Schouten, Ossebaar, et al., 2007). However, the presence of IRD in the sediments deposited during H-events in the Alboran Sea has not been observed, suggesting that this mechanism may not explain the negative excursions in $\delta^{13}C_{org}$ observed during some cold periods.

The main cold periods such as the D/O stadials and H-events have been preceded by a Polar Front shift with the influx of less saline and fresher Atlantic waters (e.g., Sierro et al., 2005), demonstrating the high sensitivity of the western Mediterranean to Greenland climate oscillations. These periods of cooling may decrease primary productivity and preservation conditions under well-ventilated Mediterranean deep waters triggered by a strengthening of northwesterly winds over the northwestern Mediterranean (Cacho et al., 2000, 2002; Colmenero-Hidalgo et al., 2004; Incarbona et al., 2013; Moreno et al., 2004). In contrast, intensified upwelling periods have been previously described as major control for marine productivity of the three different organic-SSTs sources, that is, haptophytes, eustigmatophytes, and/or Thaumarchaeota during D/O interstadials in the Iberian Atlantic margin and the Mediterranean (Darfeuil et al., 2016; Huguet et al., 2011; Pailler & Bard, 2002). Indeed, the D/O cycles in transition with cold events recorded in the marine record GP04PC, particularly during the D/O 7-5, show abrupt and fast warming-cooling phases together with productivity variability and changes in the ARs in all the groups of lipids (Figures 8 and 9), reflecting alternations in the intensity of the upwelling season and vertical mixing in the water column during more humid conditions.

5. Conclusions

The integration for the first time of four lipid paleothermometers ($U^{K'}_{37}$, TEX^H_{86}, RI-OH', and LDI) and the resulting average organic proxy-derived SST record (Figure 7g) in the marine GP04PC sediment core from the westernmost Mediterranean provide a solid overall picture of SST changes over the last 35 kyr. All the organic derived-SST records and the $\delta^{18}O$ of planktonic foraminifera *G. bulloides* record revealed similar trends in the Alboran Sea, and point to a close connection with Greenland and the North Atlantic climate variability. Particularly relevant is the high-resolution reconstruction of the D/O events 7-3 (from 35 to 26 kyr), which are characterized by fast warming-cooling phases in the four-organic derived-SSTs and the different biomarker accumulation rates.
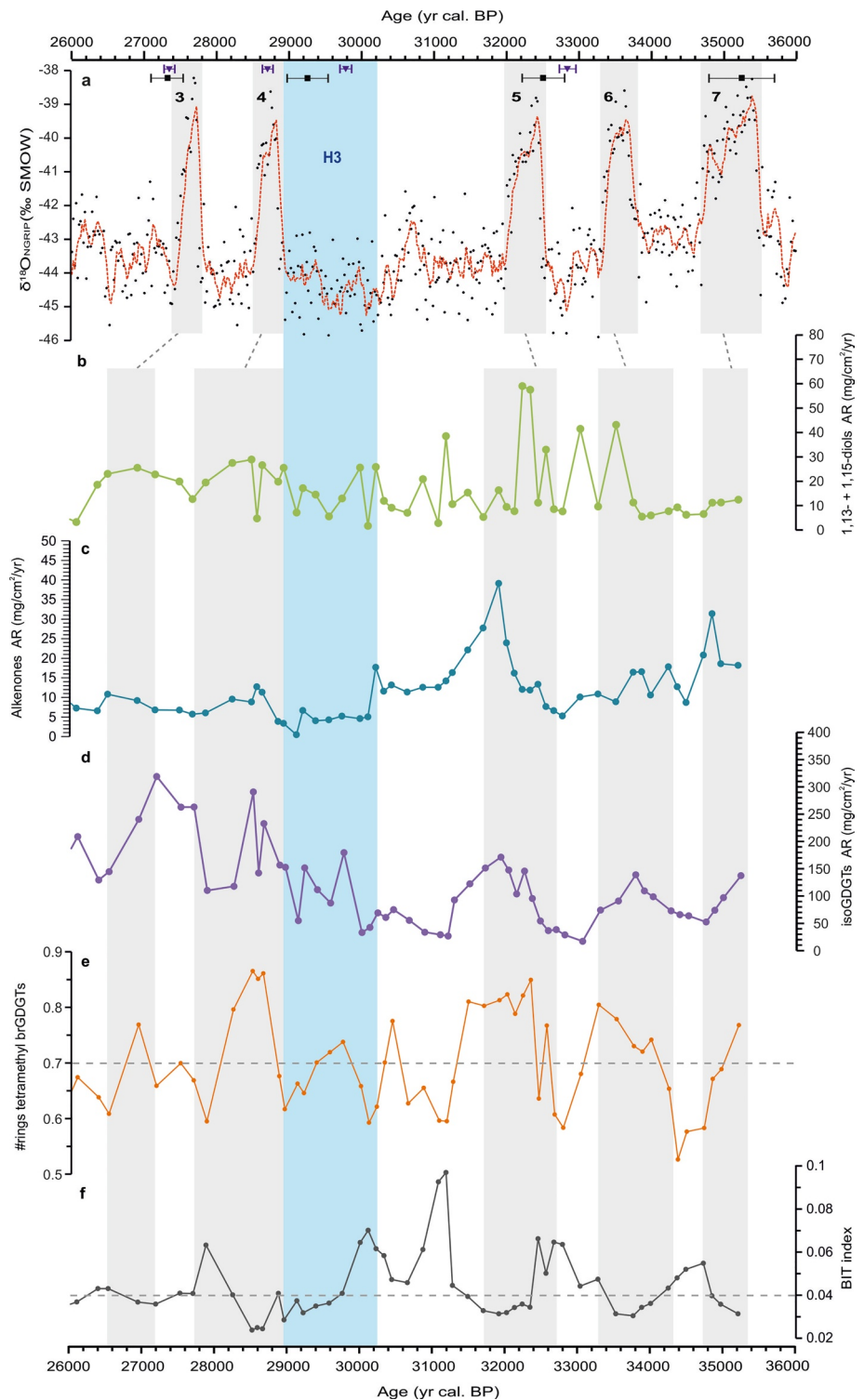
Figure 9. Proxy records from core GP04PC for the time interval between 26 and 35.2 kyr in comparison with Greenland ice core data. (a) δ^{18}O profile of Greenland NGRIP ice core (data points are black circles and the dashed red line is the 5-points running mean) (Andersen et al., 2006; Svensson et al., 2008). (b) accumulation rate (AR) of 1,13-+1,15-diols. (c) AR of the C$_{37:2}$ and C$_{37:3}$ alkenones AR, (d) AR of summed isoprenoid glycerol dialkyl glycerol tetraethers (GDGTs). (e) Average number (#rings) of tetramethylated branched GDGTs. (f) Branched and isoprenoid tetraether index. Color-coded vertical bars indicate warm and cold periods as described in Figure 8.

In general, all the organic derived-SST records showed similar temperature variations, although with substantial differences in their absolute values. TEX^H_{86}, RI-OH' and LDI-derived SST profiles start to diverge from the U^K_{37}-SST at H1 and this divergence becomes larger in the LGM and older periods; LDI-derived SSTs reach the lowest values during the H3 and the D/O stadials 5 and 6. The contribution of *Proboscia* species or freshwater eustigmatophyte algae is likely not the reason for the low LDI derived-SST during the glacial period. Thus, these differences and the lower temperature values derived by LDI, RI-OH' and TEX^H_{86}, do not seem related to contributions of different biological sources or continental organic matter, according to the biomarker distributions. LDI-SST divergences could be related to differences in the production season of eustigmatophyte algae, while TEX^H_{86} and RI-OH' could be related to changes in the predominant niche of the Thaumarchaeota during the glacial period in the Alboran Sea.

The BIT values showed an exponential correlation with the average number of rings tetramethylated brGDGTs, whereas higher BIT index values pointed to $\#rings_{tetra}$ values close to mixed terrestrial and marine GDGTs origin. However, despite the similarity of the $\delta^{13}C_{org}$ profile and the TOC content, the negative excursions in the $\delta^{13}C_{org}$ record do not agree with the maxima recorded in the brGDGTs AR profile, suggesting that fluvially-transported continental OM input did not play a substantial role in the studied marine site. In addition, the fractional abundance of C_{32} 1,15-diol range between typical values of primary marine source described from open marine settings. Furthermore, the ARs of Thaumarchaeota-derived GDGTs and other primary producers clearly reflected the D/O cycles, with productivity during D/O interstadials 7-3, and the warm B-A period.

Data Availability Statement

Dataset presented in this study is available in the open-access repository Zenodo. https://doi.org/10.5281/zenodo.4692646.

References

Abrantes, F., Voelker, A., Sierro, F. J., Naughton, F., Rodrigues, T., Cacho, I., et al. (2012). Paleoclimate variability in the Mediterranean region. In P. Lionello (Ed.), *The climate of the Mediterranean region* (pp. 1–86). Elsevier. https://doi.org/10.1016/B978-0-12-416042-2.00001-X

Andersen, K. K., Svensson, A., Johnsen, S. J., Rasmussen, S. O., Bigler, M., Röthlisberger, R., et al. (2006). The Greenland ice core chronology 2005, 15–42 ka. Part 1: Constructing the time scale. *Quaternary Science Reviews*, *25*, 3246–3257. https://doi.org/10.1016/j.quascirev.2006.08.002

Ausín, B., Flores, J. A., Sierro, F. J., Bárcena, M. A., Hernández-Almeida, I., Francés, G., et al. (2015). Coccolithophore productivity and surface water dynamics in the Alboran Sea during the last 25 kyr. *Palaeogeography, Palaeoclimatology, Palaeoecology*, *418*, 126–140. https://doi.org/10.1016/j.palaeo.2014.11.011

Balzano, S., Lattaud, J., Villanueva, L., Rampen, S., Brussaard, P. D., van Bleijswijk, J., et al. (2018). A quest for the biological sources of the ubiquitous long chain alkyl diols in the marine realm. *Biogeosciences*, *15*, 5951–5968. https://doi.org/10.5194/bg-15-5951-2018

de Bar, M. W., Dorhout, D. J. C., Hopmans, E. C., Rampen, S. W., Sinninghe Damsté, J. S., & Schouten, S. (2016). Constraints on the application of long chain diol proxies in the Iberian Atlantic margin. *Organic Geochemistry*, *101*, 184–195. https://doi.org/10.1016/j.orggeochem.2016.09.005

de Bar, M. W., Dorhout, D. J. C., Hopmans, E. C., Rampen, S. W., Sinninghe Damsté, J. S., & Schouten, S. (2019). Constraining the applicability of organic paleotemperature proxies for the last 90 Myrs. *Organic Geochemistry*, *128*, 122–136. https://doi.org/10.1016/j.orggeochem.2018.12.005

de Bar, M. W., de Nooijer, L. J., Schouten, S., Ziegler, M., Sluijs, A., & Reichart, G.-J. (2019). Comparing Seawater Temperature Proxy Records for the Past 90 Myrs From the Shallow Shelf Record Bass River, New Jersey. *Paleoceanography and Paleoclimatology*, *34*, 455–475. https://doi.org/10.1029/2018PA003453

de Bar, M. W., Weiss, G., Yildiz, C., Rampen, S. W., Lattaud, J., Bale, N. J., et al. (2020). Global temperature calibration of the Long chain Diol Index in marine surface sediments. *Organic Geochemistry*, *142*, 103983. https://doi.org/10.1016/j.orggeochem.2020.103983

Bárcena, M. A., Flores, J. A., Sierro, F. J., Pérez-Folgado, M., Fabres, J., Calafat, A., & Canals, M. (2004). Planktonic response to main oceanographic changes in the Alboran Sea (Western Mediterranean) as documented in sediment traps and surface sediments. *Marine Micropaleontology*, *53*, 423–445. https://doi.org/10.1016/j.marmicro.2004.09.009

Bazzicalupo, P., Maiorano, P., Girone, A., Marino, M., Combourieu Nebout, N., & Incarbona, A. (2018). High-frequency climate fluctuations over the last deglaciation in the Alboran Sea, Western Mediterranean: Evidence from calcareous plankton assemblages. *Palaeogeography, Palaeoclimatology, Palaeoecology*, *506*, 226–241. https://doi.org/10.1016/j.palaeo.2018.06.042

Becker, K. W., Lipp, J. S., Versteegh, G. J. M., Wörmer, L., & Hinrichs, K.-U. (2015). Rapid and simultaneous analysis of three molecular sea surface temperature proxies and application to sediments from the Sea of Marmara. *Organic Geochemistry*, *85*, 42–53. https://doi.org/10.1016/j.orggeochem.2015.04.008

Besseling, M. A., Hopmans, E. C., Koenen, M., van der Meer, M. T. J., Vreugdenhil, S., Schouten, S., et al. (2019). Depth-related differences in archaeal populations impact the isoprenoid tetraether lipid composition of the Mediterranean Sea water column. *Organic Geochemistry*, *135*, 16–31. https://doi.org/10.1016/j.orggeochem.2019.06.008

Blaauw, M., & Christen, J. A. (2011). Flexible paleoclimate age-depth models using an autoregressive gamma process. *Bayesian Analysis*, *6*, 457–474. https://doi.org/10.1214/ba/1339616472

Bond, G., Broecker, W., Johnsen, S., McManus, J., Labeyrie, L., Jouzel, J., & Bonani, G. (1993). Correlations between climate records from North Atlantic sediments and Greenland ice. *Nature*, *365*, 143–147. https://doi.org/10.1038/365143a0

Bond, G., Heinrich, H., Broecker, W., Labeyrie, L., McManus, J., Andrew, J., et al. (1992). Evidence for massive discharges of iceberg into the North Atlantic Ocean during the last glacial period. *Letters to Nature*, *360*, 245–249. https://doi.org/10.1038/360245a0

Boussetta, S., Kallel, N., Bassinot, F., Labeyrie, L., Duplessy, J.-C., Caillon, N., et al. (2012). Mg/Ca-paleothermometry in the western Mediterranean Sea on planktonic foraminifer species *Globigerina bulloides*: Constraints and implications. *Comptes Rendus Geoscience*, *344*, 267–276. https://doi.org/10.1016/j.crte.2012.02.001

Brassell, S. C., Eglinton, G., Marlowe, I. T., Pflaumann, U., & Sarnthein, M. (1986). Molecular stratigraphy: A new tool for climatic assessment. *Nature*, *320*, 129–133. https://doi.org/10.1038/320129a0

Broecker, W. S. (1994). Massive iceberg discharges as triggers for global climate change. *Nature*, *372*, 421–424. https://doi.org/10.1038/372421a0

Cacho, I., Grimalt, J., Canals, M., Sbaffi, N., & Schönfeld, R. (2001). Variability of the western Mediterranean Sea surface temperature during the last 25,000 years and its connection with the Northern Hemisphere climate changes. *Paleoceanography*, *16*, 40–52. https://doi.org/10.1029/2000pa000502

Cacho, I., Grimalt, J. O., & Canals, M. (2002). Response of the Western Mediterranean Sea to rapid climatic variability during the last 50,000 years: A molecular biomarker approach. *Journal of Marine Systems*, *33*(34), 253–272. https://doi.org/10.1016/S0924-7963(02)00061-1

Cacho, I., Grimalt, J. O., Pelejero, C., Canals, M., Sierro, F. J., Flores, J. A., & Shackleton, N. (1999). Dansgaard-Oeschger and Heinrich event imprints in Alboran Sea paleotemperatures. *Paleoceanography*, *14*, 698–705. https://doi.org/10.1029/1999PA900044

Cacho, I., Grimalt, J. O., Sierro, F. J., Shackleton, N., & Canals, M. (2000). Evidence for enhanced Mediterranean thermohaline circulation during rapid climatic coolings. *Earth and Planetary Science Letters*, *183*, 417–429. https://doi.org/10.1016/S0012-821X(00)00296-X

Cacho, I., Shackleton, N., Elderfield, H., Sierro, F. J., & Grimalt, J. O. (2006). Glacial rapid variability in deep-water temperature and $\delta^{18}O$ from the Western Mediterranean Sea. *Quaternary Science Reviews*, *25*, 3294–3311. https://doi.org/10.1016/j.quascirev.2006.10.004

Castañeda, I. S., Schefuß, E., Pätzold, J., Sinninghe Damsté, J., Weldeab, S., & Schouten, S. (2010). Millennial-scale sea surface temperature changes in the eastern Mediterranean (Nile River Delta region) over the last 27,000 years. *Paleoceanography*, *25*, 1–13. https://doi.org/10.1029/2009PA001740

Català, A., Cacho, I., Frigola, J., Pena, L. D., & Lirer, F. (2019). Holocene hydrography evolution in the Alboran Sea: A multi-record and multi-proxy comparison. *Climate of the Past*, *15*, 927–942. https://doi.org/10.5194/cp-15-927-2019

Clark, P. U., Shakun, J. D., Baker, P. A., Bartlein, P. J., Brewer, S., Brook, E., et al. (2012). Global climate evolution during the last deglaciation. *Proceedings of the National Academy of Sciences*, *109*, 1134–1142.

Colmenero-Hidalgo, E., Flores, J. A., Sierro, F. J., Bárcena, M. A., Löwemark, L., Schönfeld, J., & Grimalt, J. O. (2004). Ocean surface water response to short-term climate changes revealed by coccolithophores from the Gulf of Cadiz (NE Atlantic) and Alboran Sea (W Mediterranean). *Palaeogeography, Palaeoclimatology, Palaeoecology*, *205*, 317–336. https://doi.org/10.1016/j.palaeo.2003.12.014

Combourieu Nebout, N., Peyron, O., Dormoy, I., Desprat, S., Beaudouin, C., Kotthoff, U., & Marret, F. (2009). Rapid climatic variability in the west Mediterranean during the last 25,000 years from high resolution pollen data. *Climate of the Past*, *5*, 503–521. https://doi.org/10.5194/cp-5-503-2009

Dansgaard, W., Johnsen, S. J., Clausen, H. B., Dahl-Jensen, D., Gundestrup, N. S., Hammer, C. U., et al. (1993). Evidence for general instability of past climate from a 250-kyr ice-core record. *Nature*, *364*, 218–220. https://doi.org/10.1038/364218a0

Darfeuil, S., Ménot, G., Giraud, X., Rostek, F., Tachikawa, K., Garcia, M., & Bard, É. (2016). Sea surface temperature reconstructions over the last 70 kyr off Portugal: Biomarker data and regional modeling. *Paleoceanography*, *31*, 40–65. https://doi.org/10.1002/2015PA002831

Davtian, N., Bard, E., Darfeuil, S., Ménot, G., & Rostek, F. (2021). The novel hydroxylated tetraether index RI-OH′ as a sea surface temperature proxy for the 160–45 ka BP period off the Iberian Margin. *Paleoceanography and Paleoclimatology*, *36*(3), e2020PA004077. https://doi.org/10.1029/2020PA004077

Davtian, N., Ménot, G., Fagault, Y., & Bard, E. (2019). Western Mediterranean Sea paleothermometry over the last glacial cycle based on the novel RI-OH index. *Paleoceanography and Paleoclimatology*, *34*, 616–634. https://doi.org/10.1029/2018PA003452

de Jonge, C., Hopmans, E. C., Stadnitskaia, A., Rijpstra, W. I. C., Hofland, R., Tegelaar, E., & Sinninghe Damsté, J. S. (2013). Identification of novel penta- and hexamethylated branched glycerol dialkyl glycerol tetraethers in peat using HPLC-MS2, GC-MS and GC-SMB-MS. *Organic Geochemistry*, *54*, 78–82. https://doi.org/10.1016/j.orggeochem.2012.10.004

Elling, F. J., Könneke, M., Mußmann, M., Greve, A., & Hinrichs, K.-U. (2015). Influence of temperature, pH, and salinity on membrane lipid composition and TEX_{86} of marine planktonic thaumarchaeal isolates. *Geochimica et Cosmochimica Acta*, *171*, 238–255. https://doi.org/10.1016/j.gca.2015.09.004

Elling, F. J., Könneke, M., Nicol, G. W., Stieglmeier, M., Bayer, B., Spieck, E., et al. (2017). Chemotaxonomic characterisation of the thaumarchaeal lipidome. *Environmental Microbiology*, *19*, 2681–2700. https://doi.org/10.1111/1462-2920.13759

Fabres, J., Calafat, A., Sanchez-Vidal, A., Canals, M., & Heussner, S. (2002). Composition and spatio-temporal variability of particle fluxes in the Western Alboran Gyre, Mediterranean Sea. *Journal of Marine Systems*, *33*(34), 431–456. https://doi.org/10.1016/S0924-7963(02)00070-2

Fietz, S., Ho, S. L., & Huguet, C. (2020). Archaeal membrane lipid-based paleothermometry for applications in polar oceans. *Oceanography*, *33*, 104–114. https://doi.org/10.5670/oceanog.2020.207

Fietz, S., Huguet, C., Rueda, G., Hambach, B., & Rosell-Melé, A. (2013). Hydroxylated isoprenoidal GDGTs in the Nordic Seas. *Marine Chemistry*, *152*, 1–10. https://doi.org/10.1016/J.MARCHEM.2013.02.007

Fischer, G., & Wefer, G. (1999). *Use of proxies in paleoceanography*. Springer Berlin Heidelberg. https://doi.org/10.1007/978-3-642-58646-0

Fletcher, W. J., & Sánchez Goñi, M. F. (2008). Orbital- and sub-orbital-scale climate impacts on vegetation of the western Mediterranean basin over the last 48,000 yr. *Quaternary Research*, *70*, 451–464. https://doi.org/10.1016/j.yqres.2008.07.002

García-Lafuente, J., Naranjo, C., Sammartino, S., Sánchez-Garrido, J. C., & Delgado, J. (2017). The Mediterranean outflow in the Strait of Gibraltar and its connection with upstream conditions in the Alborán Sea. *Ocean Science*, *13*, 195–207. https://doi.org/10.5194/os-13-195-2017

Gelin, F., Volkman, J. K., de Leeuw, J. W., & Sinninghe Damsté, J. S. (1997). Mid-chain hydroxy long-chain fatty acids in microalgae from the genus *Nannochloropsis*. *Phytochemistry*, *45*, 641–646. https://doi.org/10.1016/S0031-9422(97)00068-X

Gong, C., & Hollander, D. J. (1999). Evidence for differential degradation of alkenones under contrasting bottom water oxygen conditions: Implication for paleotemperature reconstruction. *Geochimica et Cosmochimica Acta*, *63*, 405–411. https://doi.org/10.1016/S0016-7037(98)00283-X

Grauel, A. L., Leider, A., Goudeau, M. L. S., Müller, I. A., Bernasconi, S. M., Hinrichs, K.-U., et al. (2013). What do SST proxies really tell us? A high-resolution multiproxy (U^{K}_{37}, TEX^{H}_{86} and foraminifera $\delta^{18}O$) study in the Gulf of Taranto, central Mediterranean Sea. *Quaternary Science Reviews*, *73*, 115–131. https://doi.org/10.1016/j.quascirev.2013.05.007

Heaton, T. J., Köhler, P., Butzin, M., Bard, E., Reimer, R. W., Austin, W. E. N., et al. (2020). Marine20-The marine radiocarbon age calibration curve (0-55,000 cal BP). *Radiocarbon*, *62*(4), 779–820. https://doi.org/10.1017/RDC.2020.68

Heinrich, H. (1988). Origin and consequences of cyclic ice rafting in the northeast Atlantic Ocean during the past 130,000 years. *Quaternary Research*, *29*, 142–152. https://doi.org/10.1016/0033-5894(88)90057-9

Hemming, S. R. (2004). Heinrich events: Massive late Pleistocene detritus layers of the North Atlantic and their global climate imprint. *Reviews of Geophysics*, *42*, 1–43. https://doi.org/10.1029/2003RG000128

Herbert, T. D. (2003). Alkenone paleotemperature determinations. In H. D. Holland, & K. K. Turekian (Eds.), *Treatise on Geochemistry* (pp. 391–432). Elsevier. https://doi.org/10.1016/B0-08-043751-6/06115-6

Hoefs, M. J., Versteegh, G. J., Rijpstra, W. I. C., de Leeuw, J. W., & Sinninghe Damsté, J. S. (1998). Postdepositional oxic degradation of alkenones: Implications for the measurement of palaeo sea surface temperatures. *Paleoceanography*, *13*, 42–49. https://doi.org/10.1029/97pa02893

Hopmans, E. C., Schouten, S., & Sinninghe Damsté, J. S. (2016). The effect of improved chromatography on GDGT-based palaeoproxies. *Organic Geochemistry*, *93*, 1–6. https://doi.org/10.1016/j.orggeochem.2015.12.006

Hopmans, E. C., Weijers, J. W. H., Schefuß, E., Herfort, L., Sinninghe Damsté, J. S., & Schouten, S. (2004). A novel proxy for terrestrial organic matter in sediments based on branched and isoprenoid tetraether lipids. *Earth and Planetary Science Letters*, *224*, 107–116. https://doi.org/10.1016/j.epsl.2004.05.012

Huguet, C., Fietz, S., & Rosell-Melé, A. (2013). Global distribution patterns of hydroxy glycerol dialkyl glycerol tetraethers. *Organic Geochemistry*, *57*, 107–118. https://doi.org/10.1016/j.orggeochem.2013.01.010

Huguet, C., Hopmans, E. C., Febo-Ayala, W., Thompson, D. H., Sinninghe Damsté, J. S., & Schouten, S. (2006). An improved method to determine the absolute abundance of glycerol dibiphytanyl glycerol tetraether lipids. *Organic Geochemistry*, *37*, 1036–1041. https://doi.org/10.1016/j.orggeochem.2006.05.008

Huguet, C., Martrat, B., Grimalt, J. O., Sinninghe Damsté, J. S., & Schouten, S. (2011). Coherent millennial-scale patterns in $U^{K'}_{37}$ and TEX^H_{86} temperature records during the penultimate interglacial-to-glacial cycle in the western Mediterranean. *Paleoceanography*, *26*, PA2218. https://doi.org/10.1029/2010PA002048

Incarbona, A., Sprovieri, M., Di Stefano, A., Di Stefano, E., Salvagio Manta, D., Pelosi, N., et al. (2013). Productivity modes in the mediterranean sea during dansgaard-oeschger (20,000-70,000 yr ago) oscillations. *Palaeogeography, Palaeoclimatology, Palaeoecology*, *392*, 128–137. https://doi.org/10.1016/j.palaeo.2013.09.023

Jiménez-Amat, P., & Zahn, R. (2015). Offset timing of climate oscillations during the last two glacial-interglacial transitions connected with large-scale freshwater perturbation. *Paleoceanography*, *30*, 768–788. https://doi.org/10.1002/2014PA002710

Johnsen, S. J., Dahl-Jensen, D., Gundestrup, N., Steffensen, J. P., Clausen, H. B., Miller, H., et al. (2001). Oxygen isotope and palaeotemperature records from six Greenland ice-core stations: Camp Century, Dye-3, GRIP, GISP2, Renland and NorthGRIP. *Journal of Quaternary Science*, *16*, 299–307. https://doi.org/10.1002/jqs.622

Jonas, A.-S., Schwark, L., & Bauersachs, T. (2017). Late Quaternary water temperature variations of the Northwest Pacific based on the lipid paleothermometers TEX^H_{86}, $U^{K'}_{37}$ and LDI. *Deep-Sea Research Part I*, *125*, 81–93. https://doi.org/10.1016/j.dsr.2017.04.018

Kaiser, J., & Arz, H. W. (2016). Sources of sedimentary biomarkers and proxies with potential paleoenvironmental significance for the Baltic Sea. *Continental Shelf Research*, *122*, 102–119. https://doi.org/10.1016/J.CSR.2016.03.020

Kang, S., Shin, K.-H., & Kim, J.-H. (2017). Occurrence and distribution of hydroxylated isoprenoid glycerol dialkyl glycerol tetraethers (OH-GDGTs) in the Han River system, South Korea. *Acta Geochimica*, *36*, 367–369. https://doi.org/10.1007/s11631-017-0165-3

Karner, M. B., DeLong, E. F., & Karl, D. M. (2001). Archaeal dominance in the mesopelagic zone of the Pacific Ocean. *Nature*, *409*, 507–510. https://doi.org/10.1038/35054051

Kim, J.-H., Huguet, C., Zonneveld, K. A. F., Versteegh, G. J. M., Roeder, W., Sinninghe Damsté, J. S., & Schouten, S. (2009). An experimental field study to test the stability of lipids used for the TEX_{86} and $U^{K'}_{37}$ palaeothermometers. *Geochimica et Cosmochimica Acta*, *73*, 2888–2898. https://doi.org/10.1016/j.gca.2009.02.030

Kim, J. H., Schouten, S., Rodrigo-Gámiz, M., Rampen, S., Marino, G., Huguet, C., et al. (2015). Influence of deep-water derived isoprenoid tetraether lipids on the TEX^H_{86} paleo-thermometer in the Mediterranean Sea. *Geochimica et Cosmochimica Acta*, *150*, 125–141. https://doi.org/10.1016/j.gca.2014.11.017

Kim, J. H., van der Meer, J., Schouten, S., Helmke, P., Willmott, V., Sangiorgi, F., et al. (2010). New indices and calibrations derived from the distribution of crenarchaeal isoprenoid tetraether lipids: Implications for past sea surface temperature reconstructions. *Geochimica et Cosmochimica Acta*, *74*, 4639–4654. https://doi.org/10.1016/j.gca.2010.05.027

Könneke, M., Bernhard, A. E., De La Torre, J. R., Walker, C. B., Waterbury, J. B., & Stahl, D. A. (2005). Isolation of an autotrophic ammonia-oxidizing marine archaeon. *Nature*, *437*, 543–546. https://doi.org/10.1038/nature03911

Krijgsman, W. (2002). The Mediterranean: Mare Nostrum of Earth Sciences. *Earth and Planetary Science Letters*, *205*, 1–12. https://doi.org/10.1016/s0012-821x(02)01008-7

Lang, N., & Wolff, E. W. (2011). Interglacial and glacial variability from the last 800 ka in marine, ice and terrestrial archives. *Climate of the Past*, *7*, 361–380. https://doi.org/10.5194/cp-7-361-2011

Lattaud, J., Kim, J.-H., De Jonge, C., Zell, C., Sinninghe Damsté, J. S., & Schouten, S. (2017). The C_{32} alkane-1,15-diol as a tracer for riverine input in coastal seas. *Geochimica et Cosmochimica Acta*, *202*, 146–158. https://doi.org/10.1016/J.GCA.2016.12.030

Lattaud, J., Kirkels, F., Peterse, F., Freymond, C. V., Eglinton, T. I., Hefter, J., et al. (2018). Long-chain diols in rivers: Distribution and potential biological sources. *Biogeosciences*, *15*, 4147–4161. https://doi.org/10.5194/bg-15-4147-2018

Lattaud, J., Lo, L., Huang, J.-J., Chou, Y.-M., Gorbarenko, S. A., Sinninghe Damsté, J. S., & Schouten, S. (2018). A comparison of Late Quaternary paleotemperature records of the central Okhotsk Sea based on organic proxies. *Paleoceanography and Paleoclimatology*, *33*, 732–744. https://doi.org/10.1029/2018PA003388

Lattaud, J., Lo, L., Zeeden, C., Liu, Y.-J., Song, S.-R., van der Meer, M. T. J., et al. (2019). A multiproxy study of past environmental changes in the Sea of Okhotsk during the last 1.5 Ma. *Organic Geochemistry*, *132*, 50–61. https://doi.org/10.1016/j.orggeochem.2019.04.003

Lionello, P. (2012). *The climate of the Mediterranean region: From the past to the future* (1st ed.). Elsevier. https://doi.org/10.1016/B978-0-12-416042-2.00009-4

Liu, X.-L., Lipp, J. S., Simpson, J. H., Lin, Y.-S., Summons, R. E., & Hinrichs, K.-U. (2012). Mono- and dihydroxyl glycerol dibiphytanyl glycerol tetraethers in marine sediments: Identification of both core and intact polar lipid forms. *Geochimica et Cosmochimica Acta*, *89*, 102–115. https://doi.org/10.1016/j.gca.2012.04.053

Lopes dos Santos, R. A., Spooner, M. I., Barrows, T. T., De Deckker, P., Sinninghe Damsté, J. S., & Schouten, S. (2013). Comparison of organic ($U^{K'}_{37}$, TEX^H_{86}, LDI) and faunal proxies (foraminiferal assemblages) for reconstruction of late Quaternary sea surface temperature variability from offshore southeastern Australia. *Paleoceanography*, *28*, 377–387. https://doi.org/10.1002/palo.20035

Lü, X., Liu, X.-L., Elling, F. J., Yang, H., Xie, S., Song, J., et al. (2015). Hydroxylated isoprenoid GDGTs in Chinese coastal seas and their potential as a paleotemperature proxy for mid-to-low latitude marginal seas. *Organic Geochemistry*, *89*(90), 31–43. https://doi.org/10.1016/j.orggeochem.2015.10.004

Macias, D., Garcia-Gorriz, E., Dosio, A., Stips, A., & Keuler, K. (2016). Obtaining the correct sea surface temperature: Bias correction of regional climate model data for the Mediterranean Sea. *Climate Dynamics*, *51*, 1095–1117. https://doi.org/10.1007/s00382-016-3049-z

Magill, C. R., Ausín, B., Wenk, P., McIntyre, C., Skinner, L., Martínez-García, A., et al. (2018). Transient hydrodynamic effects influence organic carbon signatures in marine sediments. *Nature Communications*, *9*, 4690. https://doi.org/10.1038/s41467-018-06973-w

Martínez-Ruiz, F., Kastner, M., Gallego-Torres, D., Rodrigo-Gámiz, M., Nieto-Moreno, V., & Ortega-Huertas, M. (2015). Paleoclimate and paleoceanography over the past 20,000 yr in the Mediterranean Sea Basins as indicated by sediment elemental proxies. *Quaternary Science Reviews*, *107*, 25–46. https://doi.org/10.1016/j.quascirev.2014.09.018

Martrat, B., Grimalt, J. O., Lopez-Martinez, C., Cacho, I., Sierro, F. J., Flores, J. A., et al. (2004). Abrupt temperature changes in the Western Mediterranean over the past 250,000 years. *Science*, *306*, 1762–1765. https://doi.org/10.1126/science.1101706

Martrat, B., Jimenez-Amat, P., Zahn, R., & Grimalt, J. O. (2014). Similarities and dissimilarities between the last two deglaciations and interglaciations in the North Atlantic region. *Quaternary Science Reviews*, *99*, 122–134. https://doi.org/10.1016/j.quascirev.2014.06.016

Méjanelle, L., Sanchez-Gargallo, A., Bentaleb, I., & Grimalt, J. O. (2003). Long chain n-alkyl diols, hydroxy ketones and sterols in a marine eustigmatophyte, *Nannochloropsis gaditana*, and in *Brachionus plicatilis* feeding on the algae. *Organic Geochemistry*, *34*, 527–538. https://doi.org/10.1016/S0146-6380(02)00246-2

Ménot, G., Bard, E., Rostek, F., Weijers, J. W. H., Hopmans, E. C., Schouten, S., et al. (2006). Early reactivation of European rivers during the last deglaciation. *Science*, *313*, 1623–1625.

Millot, C. (1999). Circulation in the Western Mediterranean Sea. *Journal of Marine Systems*, *20*, 423–442. https://doi.org/10.1016/s0924-7963(98)00078-5

Mollenhauer, G., Inthorn, M., Vogt, T., Zabel, M., Sinninghe Damsté, J. S., & Eglinton, T. I. (2007). Aging of marine organic matter during cross-shelf lateral transport in the Benguela upwelling system revealed by compound-specific radiocarbon dating. *Geochemistry, Geophysics, Geosystems*, *8*, Q09004. https://doi.org/10.1029/2007GC001603

Moreno, A., Cacho, I., Canals, M., Grimalt, J. O., Sánchez-Goñi, M. F., Shackleton, N., & Sierro, F. J. (2005). Links between marine and atmospheric processes oscillating on a millennial time-scale. A multi-proxy study of the last 50,000 yr from the Alboran Sea (Western Mediterranean Sea). *Quaternary Science Reviews*, *24*, 1623–1636. https://doi.org/10.1016/j.quascirev.2004.06.018

Moreno, A., Cacho, I., Canals, M., Grimalt, J. O., & Sanchez-Vidal, A. (2004). Millennial-scale variability in the productivity signal from the Alboran Sea record, Western Mediterranean Sea. *Palaeogeography, Palaeoclimatology, Palaeoecology*, *211*, 205–219. https://doi.org/10.1016/j.palaeo.2004.05.007

Müller, P. J., Kirst, G., Ruhland, G., Von Storch, I., & Rosell-Melé, A. (1998). Calibration of the alkenone paleotemperature index $U^{K'}_{37}$ based on core-tops from the eastern South Atlantic and the global ocean (60°N-60°S). *Geochimica et Cosmochimica Acta*, *62*, 1757–1771.

Nieto-Moreno, V., Martínez-Ruiz, F., Giralt, S., Jiménez-Espejo, F., Gallego-Torres, D., Rodrigo-Gámiz, M., et al. (2011). Tracking climate variability in the western Mediterranean during the Late Holocene: A multiproxy approach. *Climate of the Past*, *7*, 1395–1414. https://doi.org/10.5194/cp-7-1395-2011

Nieto-Moreno, V., Martínez-Ruiz, F., Willmott, V., García-Orellana, J., Masqué, P., & Sinninghe Damsté, J. S. (2013). Climate conditions in the westernmost Mediterranean over the last two millennia: An integrated biomarker approach. *Organic Geochemistry*, *55*, 1–10. https://doi.org/10.1016/j.orggeochem.2012.11.001

Ohkouchi, N., Eglinton, T. I., Keigwin, L. D., & Hayes, J. M. (2002). Spatial and temporal offsets between proxy records in a sediment drift. *Science*, *298*, 1224–1227. https://doi.org/10.1126/science.1075287

Pailler, D., & Bard, E. (2002). High frequency palaeoceanographic changes during the past 140000 yr recorded by the organic matter in sediments of the Iberian Margin. *Palaeogeography, Palaeoclimatology, Palaeoecology*, *181*, 431–452. https://doi.org/10.1016/s0031-0182(01)00444-8

Pérez-Asensio, J. N., Frigola, J., Pena, L. D., Sierro, F. J., Reguera, M. I., Rodríguez-Tovar, F. J., et al. (2020). Changes in western Mediterranean thermohaline circulation in association with a deglacial Organic Rich Layer formation in the Alboran Sea. *Quaternary Science Reviews*, *228*, 106075. https://doi.org/10.1016/j.quascirev.2019.106075

Plancq, J., Grossi, V., Pittet, B., Huguet, C., Rosell-Melé, A., & Mattioli, E. (2015). Multi-proxy constraints on sapropel formation during the late Pliocene of central Mediterranean (southwest Sicily). *Earth and Planetary Science Letters*, *420*, 30–44. https://doi.org/10.1016/j.epsl.2015.03.031

Prahl, F. G., & Wakeman, S. G. (1987). Calibration of unsaturation patterns in long-chain ketone compositions for paleotemperature assessment. *Nature*, *330*, 367–369. https://doi.org/10.1038/330367a0

Rampen, S. W., Datema, M., Rodrigo-Gámiz, M., Schouten, S., Reichart, G. J., & Sinninghe Damsté, J. S. (2014). Sources and proxy potential of long chain alkyl diols in lacustrine environments. *Geochimica et Cosmochimica Acta*, *144*, 59–71. https://doi.org/10.1016/j.gca.2014.08.033

Rampen, S. W., Schouten, S., Wakeham, S. G., & Sinninghe Damsté, J. S. (2007). Seasonal and spatial variation in the sources and fluxes of long chain diols and mid-chain hydroxy methyl alkanoates in the Arabian Sea. *Organic Geochemistry*, *38*, 165–179. https://doi.org/10.1016/j.orggeochem.2006.10.008

Rampen, S. W., Willmott, V., Kim, J.-H., Rodrigo-Gámiz, M., Uliana, E., Mollenhauer, G., et al. (2014). Evaluation of long chain 1,14-alkyl diols in marine sediments as indicators for upwelling and temperature. *Organic Geochemistry*, *76*, 39–47. https://doi.org/10.1016/j.orggeochem.2014.07.012

Rampen, S. W., Willmott, V., Kim, J.-H., Uliana, E., Mollenhauer, G., Schefuß, E., et al. (2012). Long chain 1,13- and 1,15-diols as a potential proxy for palaeotemperature reconstruction. *Geochimica et Cosmochimica Acta*, *84*, 204–216. https://doi.org/10.1016/j.gca.2012.01.024

Rodrigo-Gámiz, M., Martínez-Ruiz, F., Jiménez-Espejo, F. J., Gallego-Torres, D., Nieto-Moreno, V., Romero, O., & Ariztegui, D. (2011). Impact of climate variability in the western Mediterranean during the last 20,000 years: Oceanic and atmospheric responses. *Quaternary Science Reviews*, *30*, 2018–2034. https://doi.org/10.1016/j.quascirev.2011.05.011

Rodrigo-Gámiz, M., Martínez-Ruiz, F., Rampen, S. W., Schouten, S., & Sinninghe Damsté, J. S. (2014). Sea surface temperature variations in the western Mediterranean Sea over the last 20 kyr: A dual-organic proxy ($U^{K'}_{37}$ and LDI) approach. *Paleoceanography*, *29*, 87–98. https://doi.org/10.1002/2013PA002466

Rodrigo-Gámiz, M., Martínez-Ruiz, F., Rodríguez-Tovar, F. J., Pardo-Igúzquiza, E., & Ortega-Huertas, M. (2018). Appraising timing response of paleoenvironmental proxies to the Bond cycle in the western Mediterranean over the last 20 kyr. *Climate Dynamics*, *50*, 2925–2934. https://doi.org/10.1007/s00382-017-3782-y

Rodrigo-Gámiz, M., Rampen, S. W., De Haas, H., Baas, M., Schouten, S., & Sinninghe Damsté, J. S. (2015). Constraints on the applicability of the organic temperature proxies $U^{K'}_{37}$, TEX_{86} and LDI in the subpolar region around Iceland. *Biogeosciences*, *12*, 6573–6590. https://doi.org/10.5194/bg-12-6573-2015

Sanchez-Vidal, A., Calafat, A., Canals, M., & Canals, J. (2004). Particle fluxes in the Almeria-Oran Front: Control by coastal upwelling and sea surface circulation. *Journal of Marine Systems*, *52*, 89–103. https://doi.org/10.1016/j.jmarsys.2004.01.010

Sarhan, T., Lafuente, J. G., Vargas, M., Vargas, J. M., & Plaza, F. (2000). Upwelling mechanisms in the northwestern Alboran Sea. *Journal of Marine Systems*, *23*, 317–331. https://doi.org/10.1016/s0924-7963(99)00068-8

Schouten, S., Hopmans, E. C., Schefuß, E., & Sinninghe Damsté, J. S. (2002). Distributional variations in marine crenarchaeotal membrane lipids: A new tool for reconstructing ancient sea water temperatures? *Earth and Planetary Science Letters*, *204*, 265–274. https://doi.org/10.1016/S0012-821X(02)00979-2

Schouten, S., Hopmans, E. C., & Sinninghe Damsté, J. S. (2004). The effect of maturity and depositional redox conditions on archaeal tetraether lipid palaeothermometry. *Organic Geochemistry*, *35*, 567–571. https://doi.org/10.1016/j.orggeochem.2004.01.012

Schouten, S., Huguet, C., Hopmans, E. C., Kienhuis, M. V. M., & Sinninghe Damsté, J. S. (2007). Analytical methodology for TEX$_{86}$ paleothermometry by high-performance liquid chromatography/atmospheric pressure chemical ionization-mass spectrometry. *Analytical Chemistry*, *79*, 2940–2944. https://doi.org/10.1021/ac062339v

Schouten, S., Ossebaar, J., Brummer, G. J., Elderfield, H., & Sinninghe Damsté, J. S. (2007). Transport of terrestrial organic matter to the deep North Atlantic Ocean by ice rafting. *Organic Geochemistry*, *38*, 1161–1168. https://doi.org/10.1016/j.orggeochem.2007.02.012

Schulz, H.-M., Schöner, A., & Emeis, K.-C. (2000). Long-chain alkenone patterns in the Baltic sea-an ocean-freshwater transition. *Geochimica et Cosmochimica Acta*, *64*, 469–477. https://doi.org/10.1016/S0016-7037(99)00332-4

Sierro, F. J., Hodell, D. A., Curtis, J. H., Flores, J. A., Reguera, I., Colmenero-Hidalgo, E., et al. (2005). Impact of iceberg melting on Mediterranean thermohaline circulation during Heinrich events. *Paleoceanography*, *20*, PA2019. https://doi.org/10.1029/2004PA001051

Sinninghe Damsté, J. S. (2016). Spatial heterogeneity of sources of branched tetraethers in shelf systems: The geochemistry of tetraethers in the Berau River delta (Kalimantan, Indonesia). *Geochimica et Cosmochimica Acta*, *186*, 13–31. https://doi.org/10.1016/j.gca.2016.04.033

Sinninghe Damsté, J. S., Rampen, S. W., Rijpstra, I. W. C., Abbas, B., Muyzer, G., & Schouten, S. (2003). A diatomaceous origin for long-chain diols and mid-chain hydroxy methyl alkanoates widely occurring in quaternary marine sediments: Indicators for high-nutrient conditions. *Geochimica et Cosmochimica Acta*, *67*, 1339–1348. https://doi.org/10.1016/S0016-7037(02)01225-5

Sinninghe Damsté, J. S., Rijpstra, W. I. C., & Reichart, G. J. (2002). The influence of oxic degradation on the sedimentary biomarker record II. Evidence from Arabian Sea sediments. *Geochimica et Cosmochimica Acta*, *66*, 2737–2754.

Sinninghe Damsté, J. S., Schouten, S., Hopmans, E. C., van Duin, A. C. T., & Geenevasen, J. A. J. (2002). Crenarchaeol: The characteristic core glycerol dibiphytanyl glycerol tetraether membrane lipid of cosmopolitan pelagic crenarchaeota. *The Journal of Lipid Research*, *43*, 1641–1651. https://doi.org/10.1194/jlr.M200148-JLR200

Smith, M., De Deckker, P., Rogers, J., Brocks, J., Hope, J., Schmidt, S., et al. (2013). Comparison of U$^{K'}_{37}$, TEX$^{H}_{86}$ and LDI temperature proxies for reconstruction of south-east Australian ocean temperatures. *Organic Geochemistry*, *64*, 94–104. https://doi.org/10.1016/j.orggeochem.2013.08.015

Smith, R. A., Castañeda, I. S., Groeneveld, J., De Vleeschouwer, D., Henderiks, J., Christensen, B. A., et al. (2020). Plio-Pleistocene Indonesian Throughflow variability drove Eastern Indian Ocean sea surface temperatures. *Paleoceanography and Paleoclimatology*, *35*, e2020PA003872. https://doi.org/10.1029/2020PA003872

Sollai, M., Villanueva, L., Hopmans, E. C., Reichart, G. J., & Sinninghe Damsté, J. S. (2019). A combined lipidomic and 16S rRNA gene amplicon sequencing approach reveals archaeal sources of intact polar lipids in the stratified Black Sea water column. *Geobiology*, *17*(1), 91–109. https://doi.org/10.1111/gbi.12316

Svensson, A., Andersen, K. K., Bigler, M., Clausen, H. B., Dahl-Jensen, D., Davies, S. M., et al. (2008). A 60 000 year Greenland stratigraphic ice core chronology. *Climate of the Past*, *4*, 47–57. https://doi.org/10.5194/cp-4-47-2008

Ternois, Y., Sicre, M. A., Boireau, A., Conte, M. H., & Eglinton, G. (1997). Evaluation of long chain alkenones as paleo-temperature indicators in the Mediterranean Sea. *Deep-Sea Research Part I*, *44*, 271–286. https://doi.org/10.1016/s0967-0637(97)89915-3

Tierney, J. E., & Tingley, M. P. (2014). A Bayesian, spatially-varying calibration model for the TEX$_{86}$ proxy. *Geochimica et Cosmochimica Acta*, *127*, 83–106. https://doi.org/10.1016/j.gca.2013.11.026

Tierney, J. E., & Tingley, M. P. (2015). A TEX$_{86}$ surface sediment database and extended Bayesian calibration. *Scientific Data*, *2*, 150029. https://doi.org/10.1038/sdata.2015.29

Tierney, J. E., & Tingley, M. P. (2018). BAYSPLINE: A new calibration for the alkenone paleothermometer. *Paleoceanography and Paleoclimatology*, *33*, 281–301. https://doi.org/10.1002/2017PA003201

Urey, H. C. (1947). The thermodynamic properties of isotopic substances. *Journal of the Chemical Society*, 562–581. https://doi.org/10.1039/jr9470000562

Versteegh, G. J. M., Bosch, H.-J., & de Leeuw, J. W. (1997). Potential palaeoenvironmental information of C$_{24}$ to C$_{36}$ mid-chain diols, keto-ols and mid-chain hydroxy fatty acids: A critical review. *Organic Geochemistry*, *27*, 1–13. https://doi.org/10.1016/s0146-6380(97)00063-6

Versteegh, G. J. M., Jansen, J. H. F., Schneider, R. R., & De Leeuw, J. W. (2000). Mid-chain diols and keto-ols in SE Atlantic sediments: A new tool for tracing past sea surface water masses? *Geochimica et Cosmochimica Acta*, *64*, 1879–1892. https://doi.org/10.1016/S0016-7037(99)00398-1

Versteegh, G. J. M., Riegman, R., de Leeuw, J. W., & Jansen, J. H. F. (2001). U$^{K'}_{37}$ values for *Isochrysis galbana* as a function of culture temperature, light intensity and nutrient concentrations. *Organic Geochemistry*, *32*, 785–794. https://doi.org/10.1016/S0146-6380(01)00041-9

Volkman, J. K., Barrett, S. M., & Blackburn, S. I. (1999). Eustigmatophyte microalgae are potential sources of C$_{29}$ sterols, C$_{22}$-C$_{28}$ n-alcohols and C$_{28}$-C$_{32}$ n-alkyl diols in freshwater environments. *Organic Geochemistry*, *30*, 307–318. https://doi.org/10.1016/S0146-6380(99)00009-1

Volkman, J. K., Barrett, S. M., Dunstan, G. A., & Jeffrey, S. W. (1992). C$_{30}$-C$_{32}$ alkyl diols and unsaturated alcohols in microalgae of the class Eustigmatophyceae. *Organic Geochemistry*, *18*, 131–138. https://doi.org/10.1016/0146-6380(92)90150-V

Volkman, J. K., Eglinton, G., Corner, E. D. S., & Forsberg, T. E. V. (1980). Long-chain alkenes and alkenones in the marine coccolithophorid *Emiliania huxleyi*. *Phytochemistry*, *19*, 2619–2622. https://doi.org/10.1016/S0031-9422(00)83930-8

Volkman, J. K., Eglinton, G., Corner, E. D. S., & Sargent, J. R. (1980). Novel unsaturated straight-chain C$_{37}$-C$_{39}$ methyl and ethyl ketones in marine sediments and a coccolithophore *Emiliania huxleyi*. *Physics and Chemistry of the Earth*, *12*, 219–227. https://doi.org/10.1016/0079-1946(79)90106-X

Walsh, E. M., Ingalls, A. E., & Keil, R. G. (2008). Sources and transport of terrestrial organic matter in Vancouver Island fjords and the Vancouver-Washington Margin: A multiproxy approach using δ^{13}C$_{org}$, lignin phenols, and the ether lipid BIT index. *Limnology & Oceanography*, *53*, 1054–1063. https://doi.org/10.4319/lo.2008.53.3.1054

Wei, B., Jia, G., Hefter, J., Kang, M., Park, E., Wang, S., & Mollenhauer, G. (2020). Comparison of the U$^{K'}_{37}$, LDI, TEX$^{H}_{86}$, and RI-OH temperature proxies in sediments from the northern shelf of the South China Sea. *Biogeosciences*, *17*, 4489–4508. https://doi.org/10.5194/bg-17-4489-2020

Weijers, J. W. H., Schouten, S., Spaargaren, O. C., & Sinninghe Damsté, J. S. (2006). Occurrence and distribution of tetraether membrane lipids in soils: Implications for the use of the TEX$_{86}$ proxy and the BIT index. *Organic Geochemistry*, *37*, 1680–1693. https://doi.org/10.1016/j.orggeochem.2006.07.018

Wuchter, C., Abbas, B., Coolen, M. J. L., Herfort, L., van Bleijswijk, J., Timmers, P., et al. (2006). Archaeal nitrification in the ocean. *Proceedings of the National Academy of Sciences*, *103*, 12317–12322. https://doi.org/10.1073/pnas.0600756103

Wuchter, C., Schouten, S., Coolen, M. J. L., & Sinninghe Damsté, J. S. (2004). Temperature-dependent variation in the distribution of tetraether membrane lipids of marine Crenarchaeota: Implications for TEX$_{86}$ paleothermometry. *Paleoceanography*, *19*, 1–10. https://doi.org/10.1029/2004PA001041

Yang, Y., Gao, C., Dang, X., Ruan, X., Lü, X., Xie, S., et al. (2018). Assessing hydroxylated isoprenoid GDGTs as a paleothermometer for the tropical South China Sea. *Organic Geochemistry*, *115*, 156–165. https://doi.org/10.1016/j.orggeochem.2017.10.014

References From the Supporting Information

Dang, X., Yang, H., Naafs, B. D. A., Pancost, R. D., & Xie, S. (2016). Evidence of moisture control on the methylation of branched glycerol dialkyl glycerol tetraethers in semi-arid and arid soils. *Geochimica et Cosmochimica Acta*, *189*, 24–36. https://doi.org/10.1016/j.gca.2016.06.004

Sinninghe Damsté, J. S., Rijpstra, W. I. C., Hopmans, E. C., den Uijl, M. J., Weijers, J. W. H., & Schouten, S. (2018). The enigmatic structure of the crenarchaeol isomer. *Organic Geochemistry*, *124*, 22–28. https://doi.org/10.1016/j.orggeochem.2018.06.005